Zero-phase-delay connectivity increases the reliability, concordance with structure, and prognostic ability of functional connectivity metrics

Chirag Mehra[a], Ahmad Beyh[a,b], Petroula Laiou[c,d], Pilar Garces[e], Declan Murphy[a], Eva Loth[a], Flavio Dell'Acqua[a], Joshua B Ewen[f,g], Mark P Richardson[c], Jonathan O'Muircheartaigh[a,h]

a) Department of Forensic and Neurodevelopment Sciences, Institute of Psychiatry, Psychology and Neuroscience, King's College London, London, UK
b) Department of Psychiatry, Brain Health Institute, Rutgers University, Piscataway, USA
c) Department of Basic and Clinical Neuroscience, Institute of Psychiatry, Psychology and Neuroscience, King's College London, London, UK
d) Department of Biostatistics & Health Informatics, Institute of Psychiatry, Psychology and Neuroscience, King's College London, London, UK
e) Roche Pharma Research and Early Development, Neuroscience and Rare Diseases, Roche Innovation Center Basel, F. Hoffmann–La Roche Ltd., Basel, Switzerland
f) Developmental-Behavioral Pediatrics, Ann & Robert H. Lurie Children's Hospital of Chicago, Chicago, USA
g) Department of Pediatrics at Northwestern University Feinberg School of Medicine, Chicago, Illinois, USA
h) Department of Neuroimaging, King's College London, London, UK

Abstract

Zero-phase-delay synchrony between the activity of distant neural populations has been robustly observed. Nevertheless, contemporary electroencephalography and magnetencephalography functional connectivity analyses typically exclude zero-phase-delay functional connections, assuming that they are predominantly artefactual. However, the effects of excluding them on the performance of functional connectivity metrics as potential biomarkers are unknown. Here, we showed that most cortico-cortical functional connections occur with zero- or near-zero phase-delay, even where such connectivity was unlikely to be artefactual. Including, rather than excluding, zero-phase-delay connectivity increased the reliability, concordance with structural connectivity, and predictive validity (for longitudinal changes in cognition) of functional connectivity metrics. We found that excluding zero-phase-delay connections penalised functional connectivity strength between the strongest structurally connected regions: stronger structural connections led to functional connections with phase-delays closer to zero, mediated by a shorter signal propagation time. Our findings challenge generally accepted assumptions that zero-phase-exclusive methods are superior to zero-phase-inclusive methods.

Main

Populations of neurons produce oscillatory electromagnetic activity[1,2]. Through the precise synchronisation and integration of these oscillations, the brain produces cognitive function, sensory experience and behaviour[3–9]. Studying these interactions, or functional connectivity, has provided insight into several cognitive processes[10–12] and neuropsychiatric disorders[13]. Indeed, metrics derived from functional connectivity analyses have been proposed as candidate diagnostic or prognostic biomarkers for brain-based conditions[13–18].

The averaged oscillatory electromagnetic activity of neural populations can be non-invasively measured by electroencephalography (EEG) and/or magnetoencephalography[8]. Brain-regions are assumed to be functionally connected if the phase and/or amplitude[9,19] of their oscillations are statistically interdependent[20]. Functionally connected brain regions can have perfectly synchronous activity (with zero-phase-delay), or activity in one region may follow the other (producing a phase-delay). However, the extent to which measured zero-phase-delay connectivity reflects 'true' versus artefactual connectivity remains unknown.

There is robust evidence demonstrating the presence of 'true' zero-phase-delay functional connectivity, replicated across species[21–24]. Spike-train recordings[24] have demonstrated that most functional connections between homotopic interhemispheric regions occur with zero-phase-delay. Computational models suggest that "resonance-induced synchrony[25]" facilitates zero-phase-delay connectivity: bidirectional information transfer between regions acts to mutually alter their dynamics into a stable zero-phase-delay pattern. Functions dependent on zero-phase-delay connectivity include maximizing the reliability of information transmission and facilitating spike-time-dependent plasticity[25], coding and binding features of sensory objects[8,26,27], and others[28,29]. Evidence from invasive recordings also shows near-zero-phase-delay connectivity[7], describing phase-delays that are much smaller than those arising from axonal conduction delays. An exemplar function of near-zero-phase-delay connectivity is neural encoding by hippocampal place cells[30].

Artefactual functional connectivity due to signal leakage and volume conduction also occurs with zero-phase-delay[31–34] (and ±π-phase-delay), as spatial blurring in signal leakage[31,34–36] and field-spread in volume conduction[33,36,37] occur with zero- or almost-zero-time delay. This artefactual connectivity is unavoidable in electroencephalography and magnetoencephalography data. It mimics 'true' connectivity[36] and may dominate the pattern of connectivity measurements[31,34].

Therefore, contemporary functional connectivity analyses typically exclude zero-phase-delay (and ±π-phase-delay) connections, prioritising the goal of limiting artefactual connectivity due to signal leakage and volume conduction[38,39]. However, the extent to which biologically relevant 'true' connectivity is also lost when excluding zero-phase-delay connectivity is unknown. Including versus excluding zero-phase-delay connectivity may substantially alter the conclusions drawn from otherwise identical signals[40], hindering progress in biomarker discovery (for example[41]). No study, to our knowledge, has systematically assessed the effect of including versus excluding zero-

phase-delay connections on the performance of functional connectivity metrics as candidate biomarkers.

Here, using empirical EEG data, we used a novel approach to quantify the proportion of zero- and near-zero phase-delay connectivity when signal leakage artefact was likely negligible. Then, we compared the effects of including versus excluding zero-phase-delay functional connectivity on properties desired in biomarkers: high test-retest reliability[42] and convergence with underlying biology[43]. Finally, we compared the performance of functional connectivity metrics derived from zero-phase inclusive versus exclusive methods as prognostic biomarkers for longitudinal changes in cognitive abilities. Thus, our analyses leveraged multiple performance criteria not trivially correlated with each other.

Results

We included 153 neurotypical participants (33% female), aged 6-31 years, from five study sites of the AIMS-2-TRIALS Longitudinal European Autism Project[44,45]. Participants underwent eyes-closed resting state EEG and T1-weighted and diffusion weighted MRI scans. Twenty-second EEG epochs were used to create functional connectivity networks in source space. Source reconstruction was performed using linearly constrained minimum variance beamformer[36]. Structural and functional connectivity matrices were constructed in individual-participant T1-weighted MRI space, parcellated into 68 cortical regions[46].

Note that 'true' ±π-phase-delay functional connectivity also occurs between region-pairs where 'true' zero-phase-delay connectivity is prevalent[21,47,48], and has important functions[21,47–49]. As ±π-phase-delay functional connectivity is also excluded by zero-phase-exclusive functional connectivity methods, for brevity, zero-phase-delay and π-phase-delay are subsequently referred to together as 'zero-phase-delay.'

Most functional connectivity occurs with zero- and near-zero phase-delay, even when artefactual connectivity is likely negligible

We quantified the distribution of the average phase-delay of functional connectivity between brain region-pairs (Fig. 1b). This was achieved by obtaining the instantaneous phase-delay using the Hilbert transform, for each sample in an epoch, then calculating the mean.

Between all region-pairs across all participants, most measured functional connectivity occurred with mean phase-delays of either zero-/near-zero or π-/near-π radians (near-zero/π was defined as a phase-delay < |0.3| radians from 0 or ±π radians, see Methods). Across frequency bands, alpha had the lowest proportion of zero- and near-zero phase delay connectivity (52% of all connections), while high-beta had the highest proportion (69% of all connections), Fig. 1b.

Fig. 1: Quantifying zero- and near-zero phase-delay functional connectivity

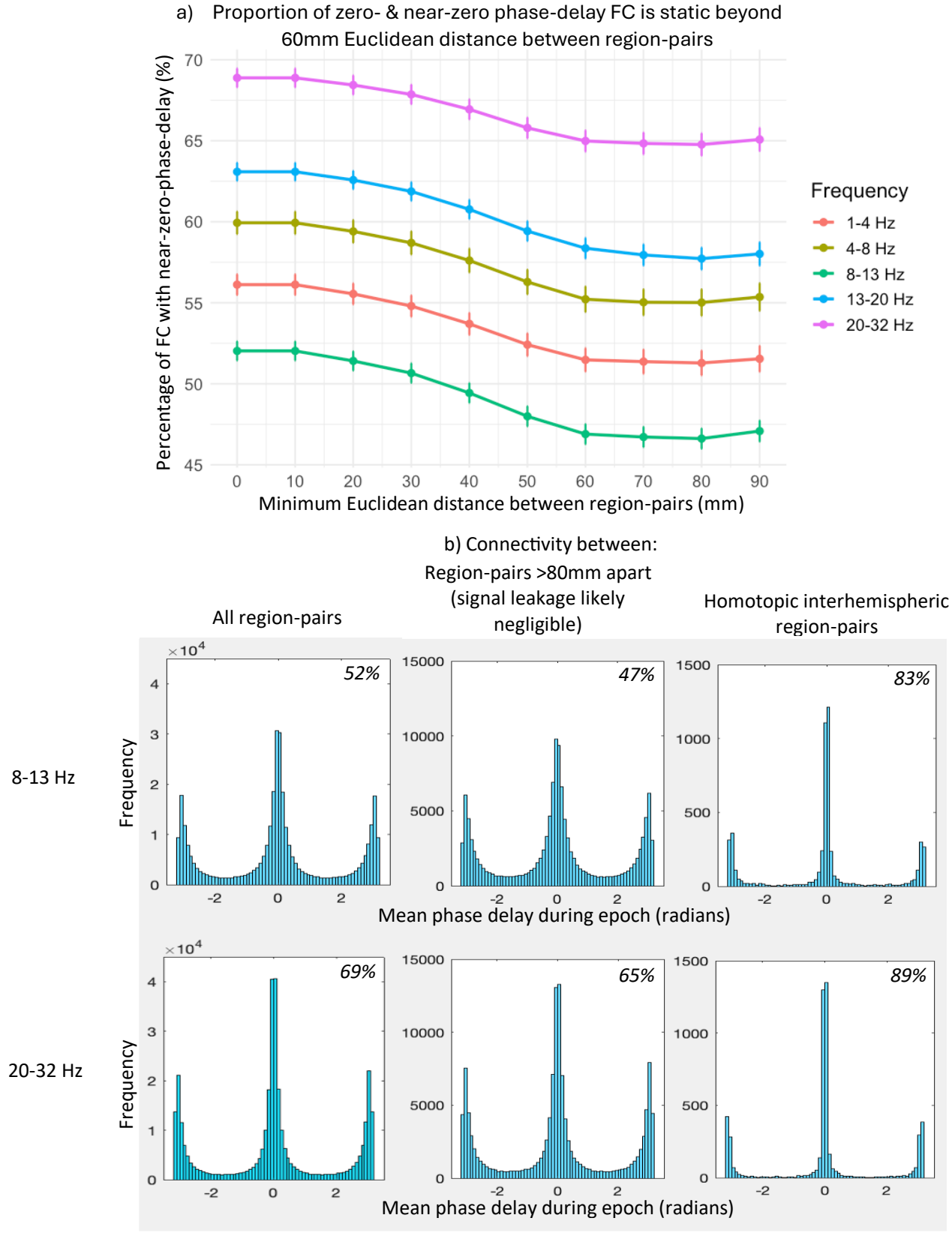

a) At distances where the percentage of zero- and near-zero phase delay connectivity no longer decreases with increasing Euclidean distance, artefactual connectivity due to signal leakage is likely to be negligible. This was found to be at Euclidean distances of ≥ 60mm for all frequency bands. Number of pairs of regions per person at each minimum distance: 0mm: 2278, 10mm: 2278, 20: 2231, 30: 2150, 40: 1966, 50: 1752, 60: 1497, 70: 1181, 80: 866, 90: 578. Mean and standard errors shown. **b)** Histograms of the average phase-delay of functional connectivity during an epoch between all region-pairs, region-pairs > 80mm Euclidean distance apart (where signal leakage is likely negligible) and between homotopic interhemispheric region-pairs. n = 153. 8-13 Hz and 20-32 Hz are the frequency bands with the lowest and highest near-zero phase delay connectivity, respectively. *Italics*: the proportion of zero- (and ±π) and near-zero (and near ±π) connectivity. FC = functional connectivity.

In source reconstructed data, signal leakage (and not volume conduction) is thought to be the primary contributor of artefactual zero-phase-delay connectivity[50]. To quantify the proportion of zero- and near-zero phase-delay functional connectivity when artefactual connectivity due to signal leakage was likely negligible, we used a novel approach. We leveraged the fact that artefactual connectivity due to signal leakage occurs at zero-phase-delay[31,51] and its influence is a function of Euclidean distance between sources[31,37,50,51]; connectivity due to signal leakage is stronger between nearby sources. Therefore, at sufficiently large distances where the percentage of zero- and near-zero phase-delay connectivity no longer decreases with increasing distance, artefactual connectivity due to signal leakage is likely to be negligible. We examined this relationship graphically (Fig. 1a), finding that the proportion of zero- and near-zero phase-delay connectivity did not vary as a function of increasing distance beyond 60mm (the lowest recorded proportion was at 80mm). This finding is consistent with artefactual connectivity due to signal leakage being likely negligible beyond 60mm, consistent with previous estimates using simulated data[36,51].

When limiting our analyses to region-pairs 80mm or more apart, we found that most functional connectivity still occurred with zero- and near-zero phase-delay, in all frequency bands except alpha (where 47% of all functional connections occurred with zero- or near-zero phase-delay, Fig. 1b).

Finally, we looked at homotopic interhemispheric functional connectivity as an example of connectivity known to robustly occur across species and measurement modalities[21,24,52,53]. Remarkably, 83-89% of homotopic interhemispheric connectivity occurred with zero- or near-zero phase-delays (Fig. 1b), despite the significant Euclidean distance between them. This proportion was greater than that of 34 randomly selected pairs of heterotopic interhemispheric region-pairs, in each frequency band (e.g. alpha: X^2 (1, n = 5,202) = 8.19, p = .0042, Supplementary Table S1).

Comparing the performance of zero-phase inclusive versus exclusive functional connectivity metrics

We limited our selection of methods for comparison to those that characterise functional connectivity based on phase relationships, amplitude relationships, or a combination thereof; do not make assumptions about directionality of connectivity based on the sign of phase difference[54]; are bivariate; and are commonly used. Thus, we selected phase locking value[55] (PLV), amplitude envelope correlation[56] (AEC) and coherence[57] as zero-phase-delay inclusive methods. We selected their methodologically corresponding zero-phase-delay exclusive methods: weighted phase

lag index[58] (wPLI), orthogonalized amplitude envelope correlation[56] (Orth AEC) and the imaginary part of coherency[33] (Img COH), respectively.

Test-retest reliability is higher in zero-phase inclusive than exclusive connectivity methods
We measured the intrasession test-retest reliability between two epochs recorded between 1-3 minutes of each other (n = 99). We measured edgewise absolute agreement using the intraclass correlation coefficient (2,1; ICC). In the alpha band, median edgewise ICC values were 0.20 – 0.71 across zero-phase-inclusive methods and 0.07 – 0.17 across zero-phase-exclusive methods (Fig. 2, Supplementary Table S2). Absolute agreement was greatest in high-beta for all zero-phase-inclusive methods and Img COH. It was highest in alpha for the wPLI and in low-beta for Orth AEC. The same patterns were also found for the consistency of each measure (Supplementary Table S3).

We found high absolute agreement for measured connectivity between region-pairs with a small Euclidean distance between them using zero-phase inclusive but not exclusive methods (Fig. 2). There are two plausible causes for this: 1) neighbouring region-pairs reliably (structurally and functionally) connect to each other[52,59,60], and this functional connectivity occurs with zero- and near-zero phase-delays and 2) artefactual connectivity[31].

Absolute agreement at homotopic interhemispheric region-pairs (Fig. 2) was high in all zero-phase inclusive methods, moderate with Img COH, and low with the Orth AEC and wPLI.

The relative test-retest reliability quantities across methods[38,61] and frequency bands[62] is consistent with previous work, despite methodological differences.

Fig. 2: edgewise absolute agreement across functional connectivity methods and frequency bands

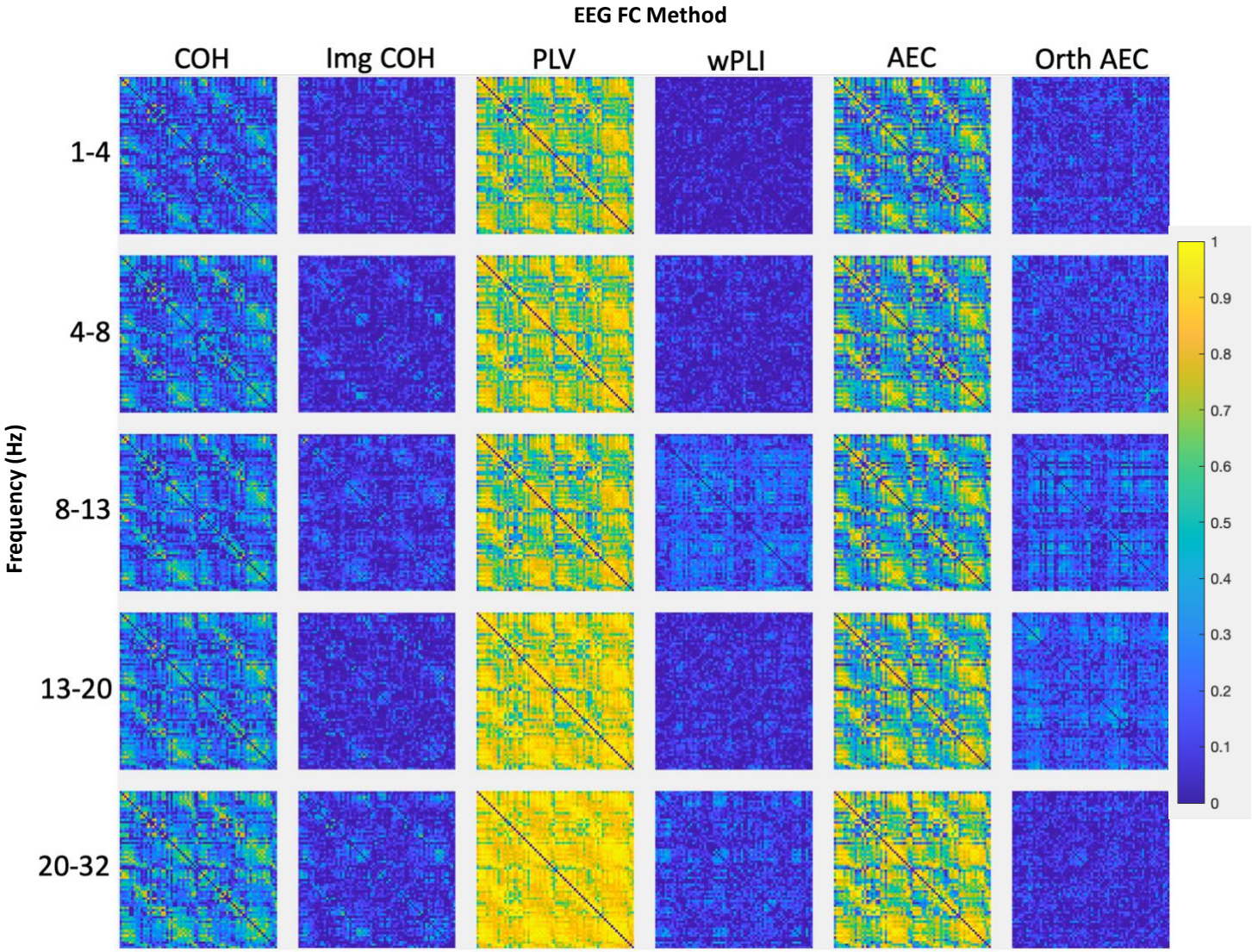

Edgewise absolute agreement, quantified by intraclass correlation coefficient (ICC), for each functional connectivity method. In 8 - 13 Hz, for example, median ICC values were 0.20 – 0.71 across zero-phase-inclusive methods versus 0.07 – 0.17 across zero-phase-exclusive methods. High absolute agreement was seen between homotopic interhemispheric region-pairs (off-diagonal edges in the adjacency matrix) in zero-phase-inclusive but not exclusive methods. High absolute agreement was seen between adjacent regions (main diagonal) in zero-phase inclusive methods, but not in zero-phase exclusive methods. Brain regions in the matrices were ordered by lobe and their proximity to each other. The colour bar denotes the edgewise ICC value. Negative ICC values were limited at 0.

Convergence with underlying neurobiology

We assessed the extent to which metrics derived from each functional connectivity method converged with underlying neurobiology by quantifying: 1) structure-function concordance (as functional connectivity is influenced by monosynaptic structural cortico-cortical pathways[60,63–66]), 2) the ability of functional connectivity metrics to capture homotopic interhemispheric connectivity, 3) their ability to predict participant age.

Concordance with structural connectivity is greater in zero-phase-inclusive methods

We measured structure-function concordance by correlating functional and structural connectivity matrices from each participant (n = 50, from 2 study sites). Structural connectivity was determined by streamline count, using diffusion weighted magnetic resonance imaging (MRI) data, analysed using spherical deconvolution tractography (2mm resolution, b-value of 1500 s/mm^2, 60 directions).

For all zero-phase-delay inclusive methods, mean structure-function concordance was significantly greater than zero in every frequency band (one-sample t-test or Wilcoxon signed-rank test, $\mu = 0$, $p < .0001$, Bonferroni corrected), Fig. 3. Concordance was not significantly different to zero for wPLI and orthogonalized AEC (one-sample t-test, $p > .05$). Surprisingly, concordance was significantly less than zero for Img COH (one-sample t-test or Wilcoxon signed-rank test, $p < .0001$, Bonferroni corrected), Fig. 3a-b. Concordance for each zero-phase-delay inclusive method was significantly higher than that for its methodologically corresponding zero-phase-delay exclusive method (paired-samples t-test or Wilcoxon signed-rank test, $p < .0001$, Bonferroni corrected, Fig. 3a-b). All findings were replicated when analysing each of the two sites separately (despite a difference in mean age between sites and large site effects in MRI analyses[67]), Supplementary Table S4a-b.

Fig. 3: Structure-function concordance is higher in zero-phase inclusive versus exclusive methods

a)

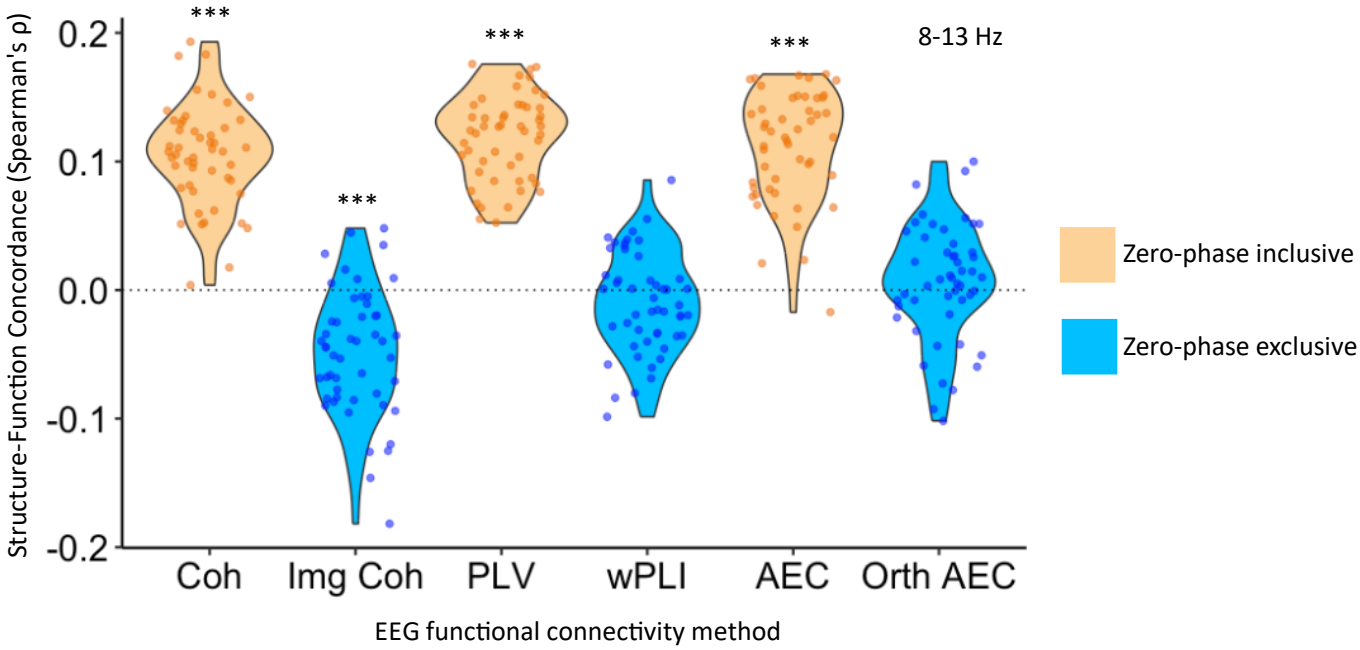

b)

0-phase inclusive method	Freq (Hz)	Mean SFC	SD	0-phase exclusive method	Freq (Hz)	Mean SFC	SD
Coherence	1 - 4[w]	.098***	.043	Imaginary part of Coherency	1 - 4	-.038***	.039
	4 - 8	.108***	.040		4 - 8	-.061***	.048
	8 - 13	.105***	.039		8 - 13	-.048***	.049
	13 - 20	.106***	.045		13 - 20	-.055***	.051
	20 - 32	.113***	.047		20 - 32	-.072***	.048
PLV	1 - 4[w]	.129***	.038	wPLI	1 - 4	-.001	.041
	4 - 8	.128***	.037		4 - 8	-.010	.040
	8 - 13	.119***	.033		8 - 13	-.010	.039
	13 - 20	.130***	.033		13 - 20	.002	.033
	20 - 32	.132***	.037		20 - 32	.001	.044
AEC	1 - 4	.123***	.042	Orthogonalized AEC	1 - 4	.006	.035
	4 - 8	.123***	.037		4 - 8	.010	.036
	8 - 13[w]	.111***	.043		8 - 13	.006	.045
	13 - 20	.126***	.036		13 - 20	.008	.036
	20 - 32	.129***	.037		20 - 32	.005	.034

a) Structure-function concordance in the alpha band and **b)** in all frequency bands (n = 50). In all frequency bands, concordance was significantly greater than zero with zero-phase-inclusive methods (one-sided t-test or Wilcoxon sum-ranked test, $\mu = 0$, $p < .0001$, Bonferroni corrected). Concordance was not significantly different from zero for two zero-phase-exclusive methods (wPLI and orthogonalized AEC). Surprisingly, concordance was significantly less than zero for the imaginary part of coherency. Concordance for each zero-phase-inclusive method was significantly higher than that of its methodologically corresponding zero-phase-exclusive method in each frequency band (paired samples t-test or Wilcoxon signed-rank test, $p < .0001$, Bonferroni corrected). *** concordance significantly different from zero, $p < .0001$, Bonferroni corrected. [w] = data not normally distributed, therefore one-sided Wilcoxon sign-rank test performed, otherwise one-sided t-tests performed. SFC = structure-function concordance.

Homotopic interhemispheric functional connectivity is robustly present with zero-phase-inclusive but not zero-phase-exclusive methods

Homotopic interhemispheric connectivity is robustly found across species and modalities[21–24,68,69]. We examined each functional and structural connectivity method's ability to capture this fundamental brain property. We calculated the edgewise mean functional (n = 153) and structural (n = 50) connectivity strength across all participants. On visual inspection, strong homotopic interhemispheric connectivity was found with all zero-phase-inclusive functional connectivity methods (Fig. 4a) and with structural connectivity (reflecting callosal connections, Fig. 4b). No zero-phase-exclusive methods showed prominent homotopic interhemispheric connectivity. Img COH showed significantly weaker connectivity between homotopic interhemispheric region-pairs than between non-homotopic region-pairs (Fig 4a, Supplementary Table S5), which we explored in a *post hoc* analysis below. Of note, given the relatively large Euclidean distances between them (median 57mm, IQR 21-80mm), functional connectivity between homotopic region-pairs would be minimally impacted by signal leakage.

Fig. 4: Edgewise structural and functional connectivity strengths

a) Edgewise functional connectivity averaged across participants

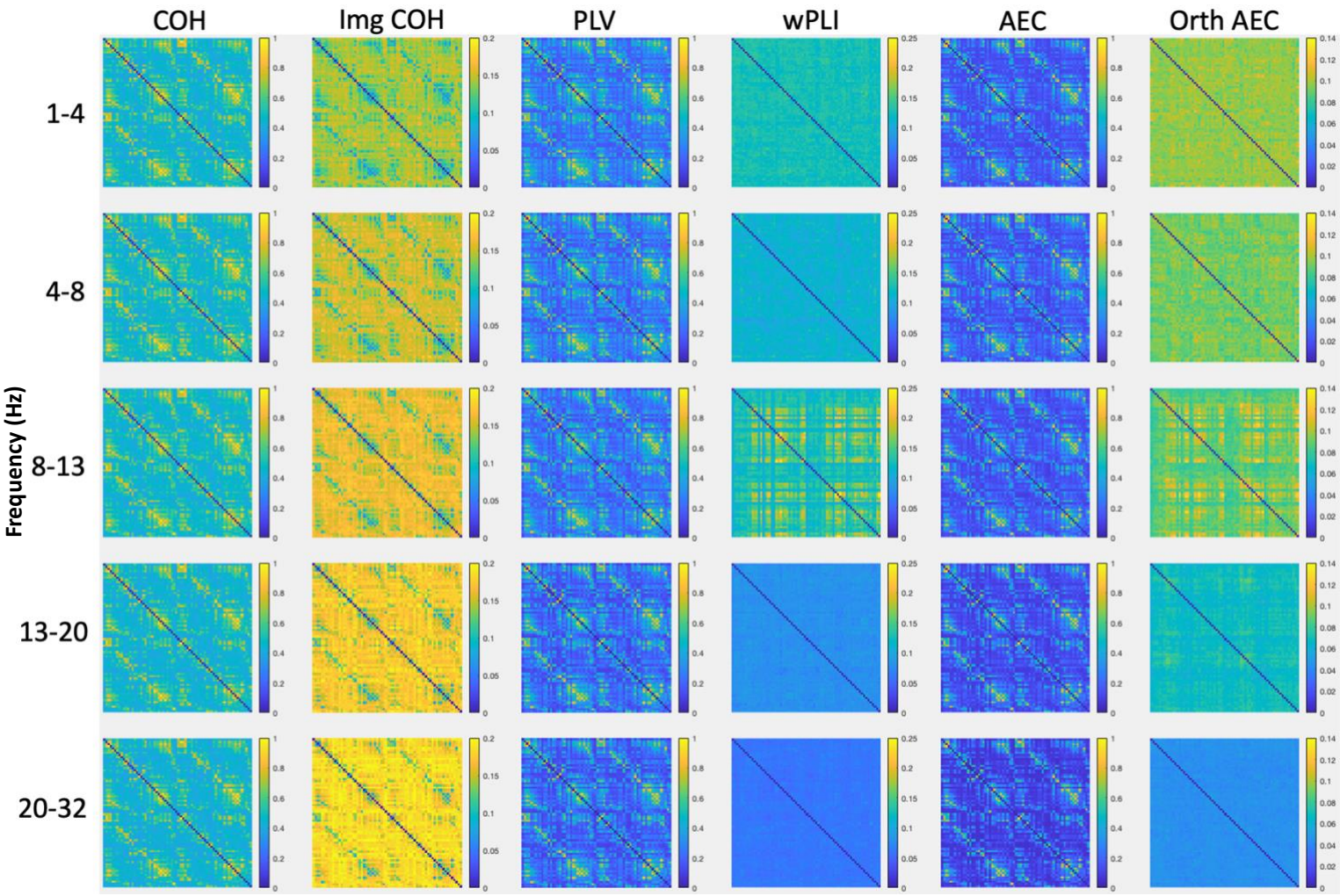

b) Edgewise structural connectivity averaged across participants

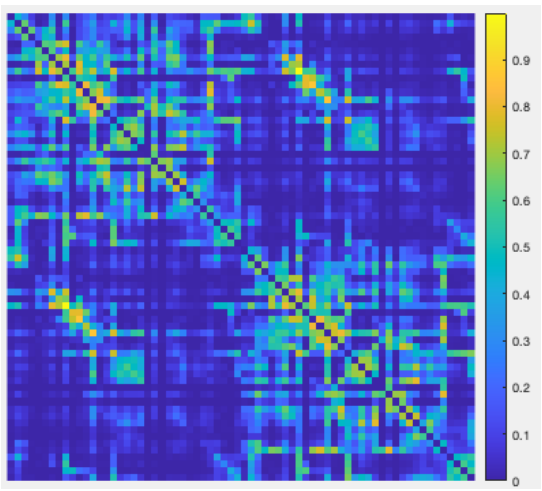

Mean edgewise **a)** EEG functional connectivity matrices (n = 153) and **b)** structural connectivity matrix (n = 50). Strong homotopic interhemispheric connectivity (seen at the off-diagonal edges in each adjacency matrix) was found with structural connectivity and with all zero-phase-inclusive functional connectivity methods. No zero-phase-exclusive methods showed prominent callosal connectivity. The imaginary part of coherency showed significantly weaker connectivity between homotopic interhemispheric region-pairs than between other region-pairs. Zero-phase-delay exclusive methods did not show strong connectivity between neighbouring region-pairs (main diagonal). Colour bars reflect connectivity strength, kept constant within each connectivity method; yellower colours denote higher connectivity strength. Brain regions in matrices are ordered by lobe and their proximity to each other.

The ability to predict current age is better in zero-phase-inclusive versus exclusive methods

Given that brain functional connectivity matures with age[70–72], we quantified the extent to which age-related changes are captured by each functional connectivity method. We assessed the ability of mean strength derived from each method to predict current age over and above head circumference (which correlates with age). First, we calculated the R^2 from 10-fold cross-validation using head circumference as the only predictor of current age (model 1, cross-validation $R^2 = .27$). Then, we added mean strength to this model (model 2). The subsequent change in R^2 (model 2 – model 1) is reported in Table 1a, n = 145. Across all frequency bands, model 2 – model 1 R^2 was greater in a zero-phase-inclusive method compared to its methodologically corresponding zero-phase-exclusive method; permutation analysis showed that this was statistically significant (false discovery rate corrected) in 10/15 comparisons.

Table 1a: Prediction of current age is greater in zero-phase inclusive versus exclusive methods. Values show model 2 – model 1 ten-fold cross validation R^2 (n = 145) for each functional connectivity method and frequency band. Model 1: *current age ~ head circumference* (model 1 cross-validation R^2 = .27). Model 2: *current age ~ head circumference + mean strength*.

Freq (Hz)	0-phase-inclusive method	Model 2 – 1 cross validation R^2	0-phase-exclusive method	Model 2 – 1 cross validation R^2	p_{FDR} permute
1 - 4	Coherence	.04	Imaginary part of Coherency	.02	.746
4 - 8		.09		.02	**.041**
8 - 13		.06		.05	.905
13 - 20		.07		-.02	**.020**
20 - 32		.01		-.01	.070
1 - 4	PLV	.05	wPLI	-.01	**.010**
4 - 8		.12		.02	**.015**
8 - 13		.16		.11	.101
13 - 20		.11		.01	**.041**
20 - 32		.10		.04	**.015**
1 - 4	AEC	.04	Orthogonalized AEC	.00	.285
4 - 8		.10		-.01	**.041**
8 - 13		.15		.02	**.000**
13 - 20		.14		.02	**.041**
20 - 32		.15		-.01	**.000**

Table 1b: Prediction of longitudinal changes in spatial working memory performance is greater in zero-phase inclusive versus exclusive methods. In models predicting longitudinal changes in spatial working memory performance, a significant main effect of functional connectivity derived pathlength was only found for coherence in the 6–12-year group and PLV in the 18-31-year group. For these models, and their corresponding zero-phase-exclusive methods, we report model 2 – model 1 leave-one-out cross-validation R^2. Model 1: *longitudinal change in spatial working memory ~ covariates*. Model 2: *longitudinal change in spatial working memory ~ covariates + functional connectivity derived pathlength*. *significant main effect of covariate in general linear model (p < .05). SWM = spatial working memory, T1 = timepoint 1, T2 = timepoint 2, PL = pathlength

Age Group	Model 1 covariates	Model 1 R^2	Covariate added in model 2:	Model 2 R^2	Model 2 – Model 1 R^2
6-12 yrs (n = 32)	Age + T1 SWM	.006	Coh PL*	.107	.101
			Img COH PL	.001	-.005
18-31 yrs (n=36)	Age + T1 SWM + T2-T1 time interval	.489	PLV PL*	.563	.074
			wPLI PL	.453	-.036

Prognostic ability for longitudinal changes in spatial working memory is higher in zero-phase inclusive versus exclusive methods

We explored the ability of metrics derived from each functional connectivity method to act as prognostic biomarkers[73] for longitudinal changes in spatial working memory ability, above and beyond current working memory abilities. We chose spatial working

memory as an outcome measure because it has highly specific associations with functional connectivity[10,12,74,75] and altered working memory is implicated in several neuropsychiatric conditions[76–78]. For each functional connectivity method, we used the weighted, normalised pathlength[79,80] between brain regions implicated in spatial working memory[81–87], in the theta band (robustly associated with working memory[11,81,82,88–90]) to predict cognitive changes between the time the EEG was recorded and a time 12-30 months in the future (mean = 19 months, SD = 3.5 months).

We found significant pathlength × age interactions in general linear models predicting changes in spatial working memory performance, when analysing all 6-31-year-old participants together (examples for coherence and Img COH provided in Supplementary Tables S6-7). Therefore, children (6-12 years, n = 32), adolescents (13-17 years, n = 41) and adults (18-31 years, n = 36) were analysed separately. Model covariates (selected using Akaike information criterion) were kept constant within each age group.

A main effect of network pathlength was only found for methods sensitive to zero-phase-delay connectivity: coherence in children ($\beta = 3.8$, SE = 1.5, $p = .014$; full model $F_{3/28} = 4.01$, $p = .017$) and PLV in adults ($\beta = -2.6$, SE = 1.1, $p = .027$; full model $F_{3/32} = 18.53$, $p = .003$), Supplementary Tables S8-9. For these statistically significant findings, we used leave-one-out cross-validation (LOOCV) to quantify model performance (Table 1b). First, we calculated the LOOCV R^2 using covariates (model 1). Then, we added weighted, normalised pathlength to this model (model 2). Model 2 – model 1 LOOCV R^2 increased by .101 for coherence in children and .074 for PLV in adults. For comparison in their methodologically corresponding zero-phase-exclusive methods, model 2 – model 1 LOOCV R^2 *decreased* by .005 for Img COH and .036 for wPLI.

Post hoc analyses

An unexpected finding from our analyses was negative structure-function concordance with Img COH. We theorised that this was because the strongest structural connections had the most 'penalised' functional connections when using Img COH, based on the following logic: stronger structural connections result in quicker (decreased) signal transmission time between region-pairs[91,92]. Quicker transmission time means that oscillatory activity at each connected region-pair occurs with smaller time-delays, and therefore, smaller phase-delays. Zero-phase-exclusive methods may penalize, rather than merely exclude, functional connectivity at near-zero-phase-delays (a salient methodological detail is that zero-phase-exclusive methods modify the connectivity strength value based on the magnitude of phase delay, while zero-phase-inclusive methods to do not). Hence, stronger structural connections may lead to weaker functional connections with some zero-phase-exclusive methods.

To test this, we hypothesised that: 1) the connectivity strength values of zero- and near-zero phase-delay connections are penalised, and not merely excluded, if derived from zero-phase-exclusive methods. 2) Stronger structural connections lead to functional connections with more penalizable phase delays, mediated by quicker possible white matter transmission time. We expected a partial mediation, as strong structural connections such as the corpus callosum also produce zero-phase-delay functional

connectivity through resonance-induced synchrony. 3) Structural connections that allow the quickest connectivity between region-pairs result in the weakest functional connectivity if derived from Img COH.

High strength functional connectivity occurs with near-zero-phase-delay and is penalised by zero-phase-delay-exclusive methods

We inspected the relationship between absolute phase delay and functional connectivity strength (n = 153), between region-pairs where signal leakage is likely negligible (region-pairs ≥80mm apart), Fig. 5. With zero-phase-inclusive methods, the median connectivity strength was significantly higher for near-zero/near-π phase-delay connectivity compared to connectivity at other phase delays, in all frequency bands (Fig. 5b). For Img COH and wPLI the opposite was true: median connectivity strength was significantly lower for near-zero/near-π phase-delay connectivity compared to connectivity at other phase delays. For orthogonalized AEC, median connectivity strength was similar between near-zero phase-delay and other phase-delay connectivity (in keeping with the milder form of orthogonalization we used, compared to others[31,93]). Therefore, zero- and near-zero phase-delay functional connectivity may be penalised, and not merely excluded, by zero-phase-exclusive methods.

Fig. 5: When signal leakage is likely negligible, most functional connectivity occurs with near-zero-phase-delay, penalised by zero-phase-exclusive methods

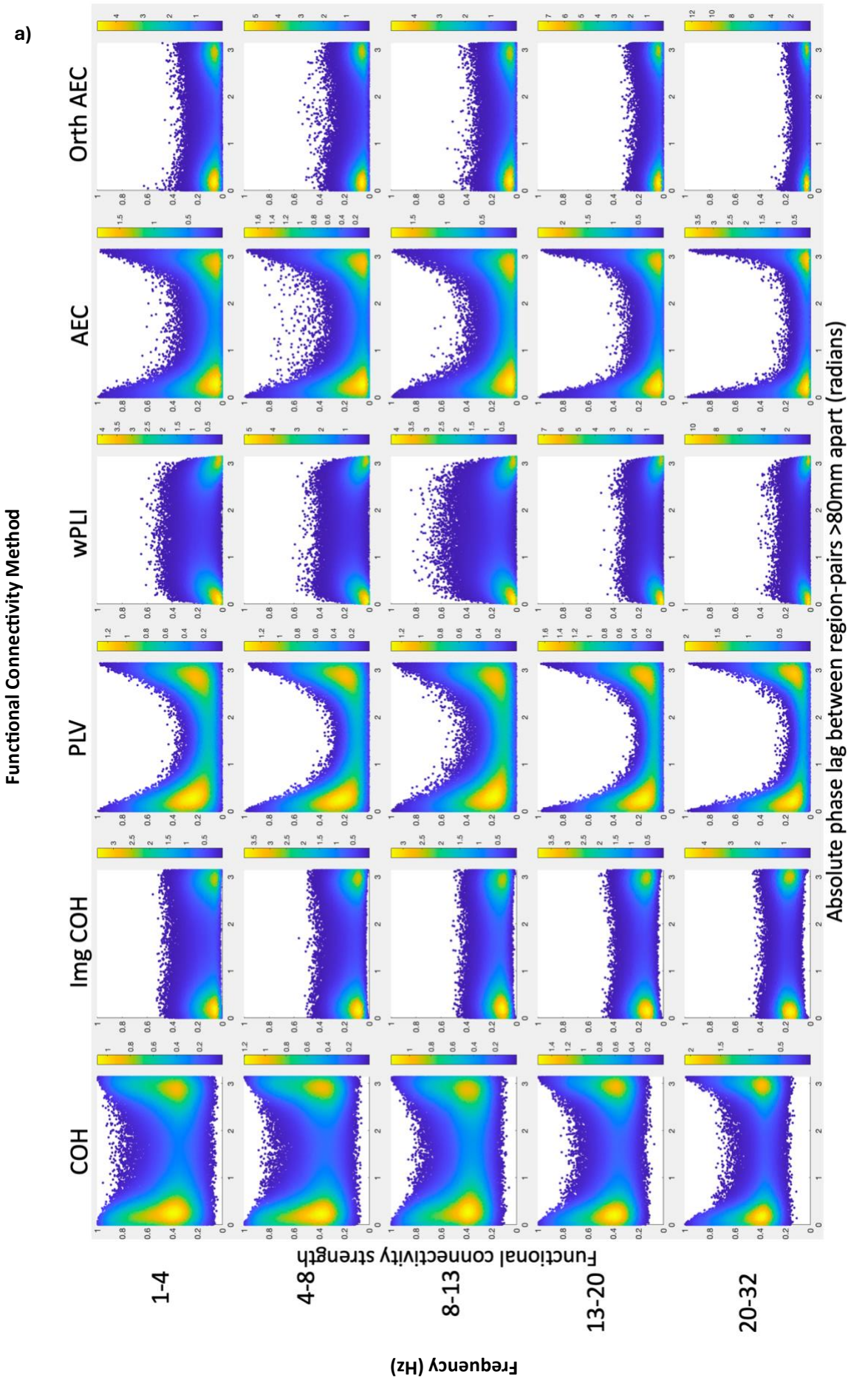

b) Comparison of the median strength of zero / near-zero versus non-near-zero phase-delay functional connectivity

0-phase-inclusive-method	Freq (Hz)	Median FC strength		0-phase-exclusive-method	Freq (Hz)	Median FC strength	
		Near-zero phase delay	Other phase delay			Near-zero phase delay	Other phase delay
Coherence	1 - 4*	.52	.39	Imaginary part of Coherency	1 - 4*	.11	.13
	4 - 8*	.52	.39		4 - 8*	.12	.15
	8 - 13*	.51	.40		8 - 13*	.14	.16
	13 - 20*	.48	.38		13 - 20*	.15	.17
	20 - 32*	.46	.37		20 - 32*	.17	.19
PLV	1 - 4*	.36	.17	wPLI	1 - 4*	.06	.16
	4 - 8*	.34	.15		4 - 8*	.06	.14
	8 - 13*	.32	.16		8 - 13*	.06	.16
	13 - 20*	.28	.11		13 - 20*	.04	.10
	20 - 32*	.26	.09		20 - 32*	.04	.08
AEC	1 - 4*	.21	.10	Orth AEC	1 - 4*	.09	.08
	4 - 8*	.22	.10		4 - 8	.08	.08
	8 - 13*	.20	.10		8 - 13	.08	.07
	13 - 20*	.17	.07		13 - 20*	.06	.06
	20 - 32*	.12	.05		20 - 32*	.04	.04

a) The relationship between absolute phase-delay and functional connectivity strength (yellower colours denote higher density of scatter points), and **b)** a comparison of edge strength when functional connectivity has zero / near-zero versus non-near-zero phase delays, for region-pairs > 80mm Euclidean distance apart (where artefactual connectivity due to signal leakage is likely negligible). For zero-phase-inclusive methods, across all frequency bands, median strength was significantly higher for near-zero-phase-delay connections compared to connections with non-near-zero-phase-delays. For the imaginary part of coherency and wPLI, across all frequency bands, the median strength was significantly lower for near-zero phase-delay connectivity compared to non-near-zero-phase-delay connectivity. For orthogonalized AEC, median strength was similar between near-zero and non-near-zero phase delay connections. Zero-phase-exclusive methods modify the connectivity strength value based on the magnitude of phase delay, while zero-phase-inclusive methods to do not. Therefore, zero-phase-exclusive methods may penalise, rather than merely exclude, zero- and near-zero phase-delay connections. * $p < .0001$, Bonferroni corrected. FC = functional connectivity.

Stronger structural connectivity leads to functional connectivity with more penalizable phase-delays, mediated by shorter white matter transmission times

We hypothesised that the stronger a structural connection, the more likely it was to produce functional connectivity with phase-delays closer to zero, penalised by zero-phase-exclusive methods. We created a penalisation scale between 0 and 1, where the most penalizable phase delays (0 and ±π) have a value of 1 and least penalizable phase delays (±π/2) have a value of zero. For each participant, we correlated their structural connectivity matrix with their penalisation scale matrix. The mean correlation between streamline count and penalisability of phase-delays was significantly greater than 0 for all frequency bands (one-sample t-test, $\mu = 0$, $p < .0001$, Bonferroni corrected), Fig. 6a. Hence, stronger structural connectivity led to functional connectivity with phase-delays more penalizable by zero-phase-exclusive methods.

To test whether this relationship was mediated by quicker signal transmission time through white matter connections, we used a proxy of signal transmission time through white matter tracts. We divided the median length (distance) of white matter tracts between region-pairs by a proxy of transmission speed. The median hindrance modulated orientational anisotropy (HMOA) was used a proxy of transmission speed, as white matter microstructural integrity can reflect myelination[94] and correlates with nerve conduction velocity[95,96]. Additionally, the transmission latencies of evoked potentials (an established method of approximating transmission speed[97]) negatively correlate with white matter microstructure across studies[92,98]. Across all frequency bands, we found that the effect of structural connectivity strength on the penalisability of the phase-delay of functional connectivity was significantly partially mediated by the proxy of white matter transmission time (e.g. proportion of the direct effect mediated by the proxy of signal transmission time was .234 [95% confidence intervals, calculated using 1000 bootstrapped samples = .197 - .270] in alpha, Fig. 6b-c). The mediation was strongest in higher frequency bands, consistent with stronger structure-function concordance in higher frequency bands in zero-phase-inclusive methods (Fig. 3b).

Fig. 3: Stronger structural connectivity leads to functional connectivity with phase-delays closer to 0 or ±π, mediated by a proxy of shorter white matter transmission time

a) Correlation between structural connectivity strength and penalisation values

Freq (Hz)	Spearman's Correlation	SD
1 - 4	.092***	.039
4 - 8	.098***	.036
8 - 13	.096***	.036
13 - 20	.092***	.031
20 - 32	.095***	.042

b)

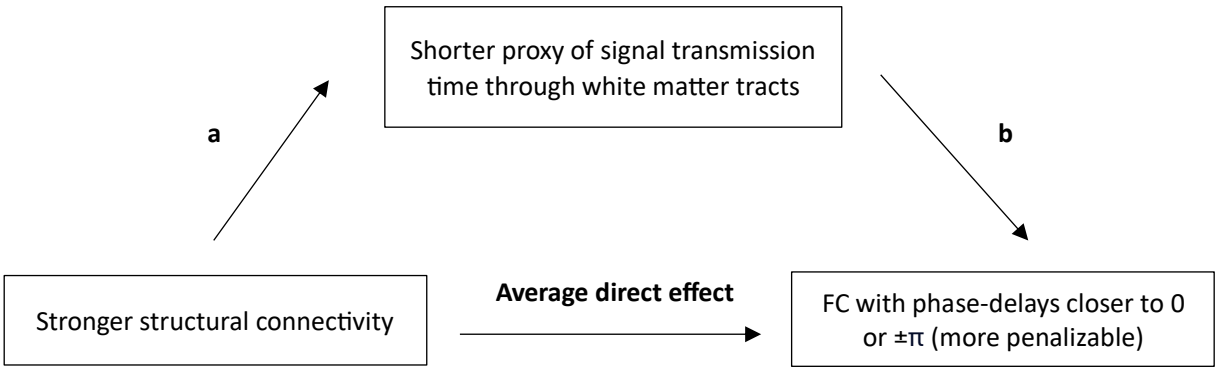

c) Mediation analysis statistics for the model in b), for each frequency band

Freq (Hz)	Total effect ($x10^{-3}$)	Average direct effect ($x10^{-3}$)	a	b ($x10^{-6}$)	Average causal mediation effect ($x10^{-3}$)	Proportion mediated [95% confidence interval]
1 – 4	2.97***	2.32***	-159***	-4.04***	0.64	.217 [.175 - .260]
4 – 8	2.61***	2.08***	-159***	-3.33***	0.53	.203 [.160 - 0.260]
8 – 13	3.86***	2.96***	-159***	-5.67***	0.90	.234 [.200 - .280]
13 – 20	2.64***	1.92***	-159***	-4.49***	0.71	.271 [.225 - .330]
20 – 32	2.17***	1.57***	-159***	-3.78***	0.60	.277 [.220 - .350]

a) We created a penalisation scale between 0 and 1, where phase-delays most penalised by zero-phase-exclusive methods (0 and ±π) have a value of 1 and phase-delays least penalised (±π/2) have a value of 0. The mean correlation across participants between streamline count and penalisability of phase-delays was significantly greater than 0 for all frequency bands, n = 50 (*** p <.0001, Bonferroni corrected, one-sample t-test, μ = 0). **b-c)** We created a proxy of signal transmission time through white matter tracts. The effect of structural connectivity strength on the penalisabiltiy of the phase-delay of functional connectivity was partially mediated by the proxy of white matter transmission time, across all frequency bands. All effects were statistically significant (*** = p < .0001, Bonferroni corrected). SD = standard deviation.

Structural connections with shorter signal transmission time are associated with weaker functional connectivity with some zero-phase-exclusive methods

We found that the shorter the proxy of signal transmission time through white matter tracts, the stronger the functional connectivity value was for all zero-phase-inclusive methods (one-sample t-test, $\mu = 0$, $p < .0001$, Bonferroni corrected), Fig. 7. This is the expected biological relationship[59,99,100]. This was also the case for the alpha band in wPLI ($p < .05$, Bonferroni corrected) and orthogonalized AEC ($p < .001$, Bonferroni corrected), but no other frequency bands when using these methods. Note that alpha has the smallest proportion of near-zero-phase-delay connectivity (Fig. 1b). For Img COH, the shorter the proxy of signal transmission time through white matter tracts, the weaker functional connectivity strength, in all frequency bands (one-sample t-test, $\mu = 0$, $p < .0001$, Bonferroni corrected). This is inconsistent with prior network literature[59,99,100].

Thus, the structural connections that are prioritised in brain through quick structural pathways may be penalised by some zero-phase-delay-exclusive functional connectivity methods.

Fig. 7: Structural connections with shorter signal transmission time are associated with weaker functional connectivity with some zero-phase-exclusive methods

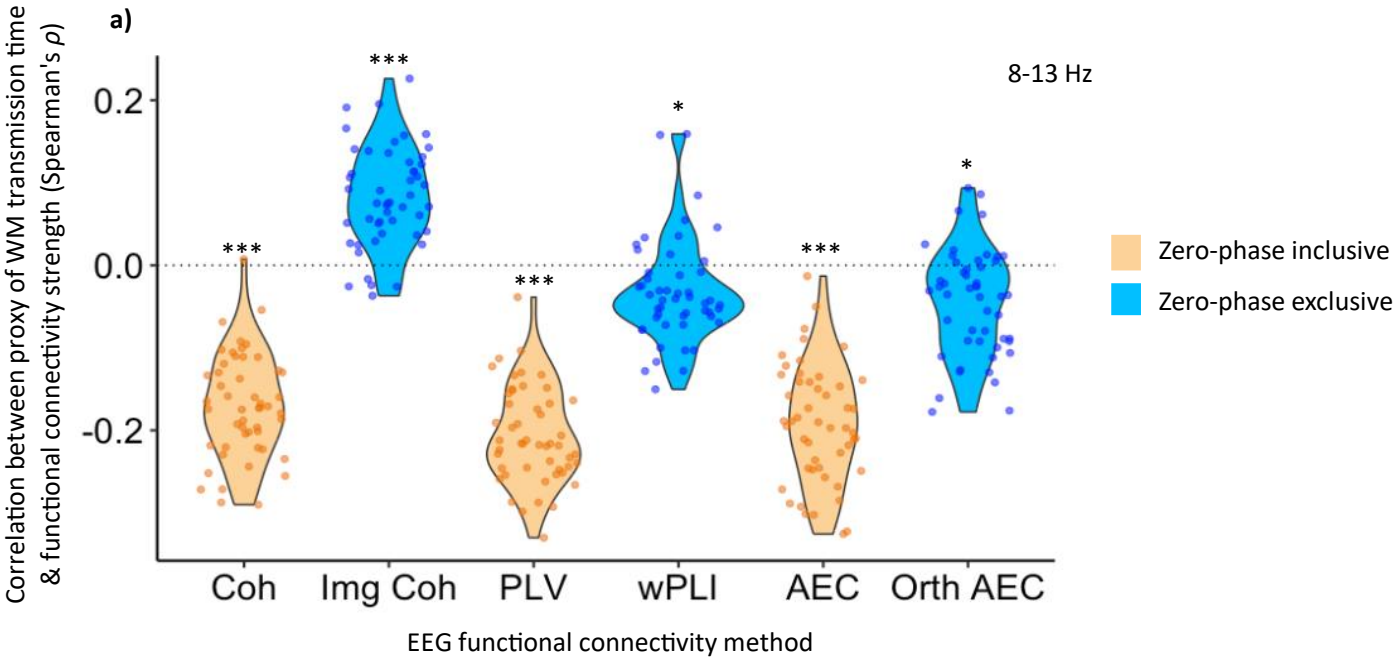

b) Spearman's correlation between the proxy of white matter signal transmission time and functional connectivity strength

0-phase-inclusive-method	Freq (Hz)	Mean correlation	SD	0-phase-exclusive-method	Freq (Hz)	Mean correlation	SD
Coherence	1 - 4	-.132***	.060	Imaginary part of Coherency	1 - 4	.051***	.062
	4 - 8	-.120***	.058		4 - 8	.078***	.062
	8 - 13	-.170***	.063		8 - 13	.083***	.060
	13 - 20	-.147***	.072		13 - 20	.071***	.070
	20 - 32	-.148***	.052		20 - 32	.087***	.067
PLV	1 - 4	-.156***	.060	wPLI	1 - 4	-.007	.053
	4 - 8	-.160***	.060		4 - 8	.004	.060
	8 - 13	-.206***	.058		8 - 13	-.033*	.062
	13 - 20	-.180***	.064		13 - 20	.000	.054
	20 - 32	-.175***	.063		20 - 32	-.005	.071
AEC	1 - 4	-.155***	.056	Orthogonalized AEC	1 - 4	-.012	.056
	4 - 8	-.163***	.063		4 - 8	-.022	.063
	8 - 13	-.192***	.071		8 - 13	-.045**	.065
	13 - 20	-.173***	.067		13 - 20	-.015	.059
	20 - 32	-.172***	.067		20 - 32	-.007	.057

We created a proxy of signal transmission time through white matter tracts. The quicker (shorter) the proxy of signal transmission time through structural connections, the stronger the functional connectivity value for all zero-phase-inclusive methods (one-sample t test, $\mu = 0$, $p < .0001$, Bonferroni corrected), **a)** shown graphically for alpha and **b)** tabulated for all frequency bands (n = 50). This was also the case for alpha (but not other frequency bands) in wPLI ($p < .05$, Bonferroni corrected) and orthogonalized AEC ($p < .001$, Bonferroni corrected). For the Img COH, the quicker the proxy of structural transmission time, the weaker functional connectivity strength, in all frequency bands (one-sample t-test, $\mu = 0$, $p < .0001$, Bonferroni corrected). Such a relationship is inconsistent with prior literature. ***$p < .0001$, **$p < .001$, *$p < .05$ (Bonferroni corrected).

Discussion

We demonstrated that most functional connectivity between cortical region-pairs occurs with zero- and near-zero phase-delay. We used a novel approach to show that this is also the case when artefactual connectivity due to signal leakage is likely negligible. Including zero- and near-zero phase-delay connectivity led to increased test-retest reliability, increased concordance with structural connectivity, and increased performance in predicting both current age and longitudinal changes in cognitive ability. Thereby, through converging lines of evidence, we show that functional connectivity metrics that include zero- and near-zero phase-delay connections have more properties desired in candidate biomarkers. We propose that the decreased structure-function concordance and predictive abilities associated with zero-phase-exclusive methods are due to their penalisation of most 'true' cortico-cortical functional connectivity.

We investigated homotopic interhemispheric connectivity as an example of structural and functional connectivity robustly found across species[21–24,68,69]. We captured conspicuous homotopic connections using structural connectivity and zero-phase-inclusive functional connectivity methods. We found that they were either inconspicuous or penalised when using zero-phase-exclusive methods. In contrast, a previous study[31] captured connectivity between sensory homotopic region-pairs using orthogonalized AEC. However, given our and others'[21,24] finding that homotopic region-pairs predominantly interact with zero- and near-zero-phase-delay, our findings are expected. We see the inability to capture this fundamental feature of brain connectivity as a key weakness of zero-phase-exclusive methods.

We found that structure-function concordance was significantly greater when using zero-phase-inclusive compared to zero-phase-exclusive methods. This is consistent with a previous small study of 17 participants[60]. Additionally, we were surprised that with some zero-phase-exclusive methods, here Img COH, the strongest structural connections paradoxically had the weakest functional connections. We showed that this was because stronger structural connectivity led to functional connectivity with phase-delays closer to zero, mediated by a proxy of shorter signal transmission times. Then, we showed that functional connectivity at near-zero-phase-delays had penalised strength when derived from some zero-phase-exclusive methods. Hence, for Img COH, we found that region-pairs connected by white matter tracts with the quickest possible signal transmission times had the weakest functional connections. This relationship is inconsistent with previous network literature[59,99,100].

Predictive validity for longitudinal changes in spatial working memory performance, as well as the ability to predict current age, was substantially greater when zero- and near-zero phase-delay connections were included. Strengths of our approach included the fact that our spatial working memory prediction findings were derived using region-pairs[81–87], the frequency band and the network topology measure known to be implicated in spatial working memory[11,81,82,88,89,101], specified *a priori*. Consistent with our findings, a small, cross-sectional prior study[102] found that including versus excluding zero-phase-delay connectivity substantially increased the variance explained in predicting current task state. It showed that predictive ability was not dependent on

differing characteristics between functional connectivity methods besides the inclusion or exclusion of zero-phase-delay connectivity; it excluded zero-phase-delay connectivity using a large-Laplacian while keeping the connectivity method constant.

Conversely, zero-phase-exclusive methods did demonstrate some advantages. In agreement with others[31,33,58], it appeared that zero-phase-exclusive methods likely minimised artefactual connectivity due to volume conduction and signal leakage: functional connectivity between neighbouring region-pairs was minimal when using them (Fig. 4). However, valid functional connections are also most commonly present between nearby region-pairs[9,65,99,103], and were not reliably captured by zero-phase-exclusive methods (Figs. 2 and 4).

Quantifying 'true' zero- and near-zero phase-delay connectivity has not been previously achieved in empirical EEG or MEG data. Our approach to identify the distance between region-pairs where the effects of signal leakage were likely negligible was novel. Previous approaches have used simulated data[36,51], with findings consistent with ours. However, simulated data cannot yet accurately inform us about the proportion of 'true' cortico-cortical functional connectivity that occurs with zero- and near-zero phase-delay, as even the most biologically realistic simulations[104] cannot accurately model the emergent properties of whole-cortex connectivity[7,24,105]. Therefore, unlike simulated data approaches, our approach can illustrate that most cortical functional connectivity occurs at zero- or near-zero phase-delay, and that excluding it has deleterious effects on the properties of biomarkers derived from functional connectivity metrics.

A key strength of our functional connectivity metric performance assessment approach was the use of convergence across performance criteria – each based on different modalities not trivially correlated with each other. Previous attempts at assessing the validity of zero-phase-inclusive versus zero-phase-exclusive methods have used single measures of functional connectivity performance[31,38,93], which may lead to bias[61,106]. Even using (only) two modalities could be misleading: for example, both structural connectivity and functional connectivity from zero-phase-inclusive methods are more reliable with decreasing Euclidean distance between region-pairs[107,108]. Thus, high structure-function concordance may reflect reliable but artefactual functional connectivity correlating with reliable and valid structural connectivity at small distances. Therefore, our use of non-neuroimaging markers of performance was important.

An additional strength was our multi-site study design; our most unexpected finding (negative structure-function concordance with Img COH) was reproduced when analysing each study site separately. Next, as a measure to assess convergence against, the structural connectome has high inter- and intra-individual reliability[63,109]. Further, to test each functional connectivity metric property, we used multiple analysis approaches, with consistent results.

Is high test-retest reliability a good measure of functional connectivity metric performance? High reliability has been used as evidence of the presence of volume conduction or signal leakage artefact in functional connectivity analyses[38]. Further, high

validity may be present with low test-retest reliability: brain-regions functionally connected at one moment may vary from the next. However, in the context of a candidate prognostic or diagnostic biomarker, high test-retest reliability is crucial; it establishes the upper limit of its predictive validity[110].

While we aimed to identify where the effects of signal leakage were negligible, the use of EEG additionally introduced volume conduction artefact[111]. In sensor space, artefactual connectivity due to volume conduction has a non-linear relationship with scalp distance[34], making it challenging to account for. However, simulated data show that when source reconstruction is applied, artefactual connectivity due to volume conduction decreases with increasing Euclidean distance[36], making our approach to determine areas of minimal signal leakage also relevant to volume conduction. Further, EEG is a ubiquitous tool in research and clinical settings[112], a strength when attempting to identify candidate biomarkers.

To some extent, our findings are surprising given the field's move towards favouring zero-phase-exclusive methods[31,33,39,113]. Zero-phase-exclusive methods were introduced to identify 'true' brain interactions as opposed to trivial artefact[33,58]. Over the last 20+ years, they have consistently been published as improvements on their corresponding zero-phase-inclusive methods. This position has been adopted by several studies attempting to identify candidate diagnostic or prognostic biomarkers[113,114 39]. Some authors have argued that zero-phase connectivity in the brain is physiologically implausible[39], despite robust evidence to the contrary.

The presence of 'true' zero-phase-delay synchrony in brain is unintuitive: action potential transmission delays due to axonal conduction and synaptic transmission are in the order of tens of milliseconds[7,23]. Such time-delays would cause substantial phase-delays between connected brain regions. Thus, zero-phase-delay functional connectivity across distant neural populations would not be possible if the brain was a simple linear system. A leading postulated mechanism for zero-phase-delay connectivity is "resonance-induced synchrony[25]". Key structures have empirically shown to facilitate the bidirectional information transfer necessary for it, including cortico-thalamo-cortical loops[7,23] and the corpus callosum[23,115,116] (however see[117]). Other hypothesised mechanisms of zero-phase-delay synchrony include entrainment[118] and emergence[119]. It is possible that multiple mechanisms work in unison[23].

The debate central to our study is the extent to which measured zero- and near-zero phase-delay connectivity in source reconstructed data is artefactual versus 'true'. We found that most functional connectivity occurred with zero- and near-zero phase-delays, even when signal leakage was likely negligible. Converging lines of evidence demonstrate that including zero-phase-delay functional connectivity increases the performance of functional connectivity metrics as biomarkers. These findings challenge generally accepted assumptions that zero-phase-exclusive methods are superior to zero-phase-inclusive methods.

Methods

Participants

We included participants from the AIMS-2-TRIALS Longitudinal European Autism Project, described here[44,45]. In this analysis, we included 153 healthy, neurotypical participants from 5 study sites. For the analyses predicting longitudinal changes in spatial working memory, participants were split into children (6-12 years, n = 41), adolescents (13-17 years, n = 50) and adults (18-31 years, n = 62), Table 2. Included participants needed at least 20 seconds of usable eyes-closed resting-state EEG data, a good quality T1-weighted (T1w) magnetic resonance spectroscopy (MRI) scan image, and a full-scale intelligence quotient ≥75. We excluded participants with diagnosed neurodevelopmental conditions, intellectual disability, neurological conditions, mental health conditions (e.g. schizophrenia, bipolar affective disorder) and significant systemic disease (e.g. auto-immune conditions). Intelligence quotient was measured by the Wechsler Abbreviated Scale of Intelligence, Second Edition[120].

Table 2 – Characteristics of included participants. This study included 153 participants aged between 6 and 31 years. For the analyses predicting longitudinal changes in spatial working memory, participants were grouped by age: children (6-12 years), adolescents (13-17 years), and adults (18-31 years).

	6-12 yrs (n = 41)	**13-17 yrs (n = 50)**	**18-31 yrs (n = 62)**	**Total (n = 153)**	***p* value**
Age (years)					
Mean (SD)	10.2 (1.9)	15.9 (1.4)	23.4 (3.5)	17.4 (6.0)	-
Range	6 - 12	13 - 18	18 – 31	6 – 31	
Sex					
Female	15 (37%)	20 (40%)	16 (26%)	51 (33%)	.25
Full Scale IQ					
Mean (SD)	111 (12)	108 (12)	109 (12)	109 (12)	.41
Range	76 – 139	77- 133	85 – 142	76 – 142	
Site					
London	12	7	24	43	< .001
Mannheim	7	18	3	28	
Nijmegen	13	17	8	38	
Rome	0	0	16	16	
Utrecht	9	8	11	28	

Electroencephalography methods

EEG data acquisition: Four segments of 30 second, eyes-closed EEG recordings were captured. These short epochs were used to maximise comfort for young participants. Data were acquired at five sites: Central Institute of Mental Health (CIMH, Mannheim, Germany), King's College London (KCL, United Kingdom), University Nijmegen Medical Centre (RUNMC, Netherlands), University Campus BioMedico (UCBM, Rome, Italy) and

University Medical Centre Utrecht (UMCU, Netherlands). The following EEG systems were employed: Brainvision (CIMH, KCL, RUNMC), Biosemi (UMCU) and Micromed (UCBM), with sampling frequencies of 5000 Hz (KCL, RUNMC), 2048 Hz (UMCU), 2000 Hz (CIMH) and 256–1000 Hz (UCBM). All sites used 10–20 layout caps, with 60–70 electrodes.

EEG artefact cleaning: EEG artefact identification and removal was performed for each 30 second epoch, as per[113]. Only data from the 61 electrodes commonly used across all sites were retained. The following steps were performed: (1) electrode channels with poor data quality were removed, (2) temporal segments with large transient artifacts such as muscle bursts or movements were discarded, (3) independent component analyses were applied using fastICA[121] to distinguish signal from noise, (4) artefactual independent components were identified and eliminated, (5) and channels discarded in (1) were interpolated. The common average signal across all channels was used as the reference. If more than 10 cannels were eliminated in step 1, the epoch was not included in subsequent analyses.

Prior to source localisation, initial downsampling and bandpass filtering were performed, as per[121]. Except for signals from UCBM (which were recorded at 256 Hz and not initially downsampled), EEG signals were downsampled to 1000 Hz, with an antialiasing filter (low-pass finite impulse response filter, Kaiser window, cutoff of 300 Hz, transition band width 100 Hz), using EEGlab[122]. Then, the entire EEG resting-state recording (all four 30 second epochs and the segments in between them), with 10 seconds of data padding, was bandpass filtered between 1–32 Hz with a finite impulse response filter of order 2000, using a Hamming window, in both forward and backward directions, with detrending , using FieldTrip[123].

Source Reconstruction: Source reconstruction was performed using individual-participant T1-weighted MRI images (acquisition parameters detailed below). T1-weighted MRIs were segmented with Statistical Parametric Mapping 12 (SPM12) software[124] into grey matter, white matter, cerebrospinal fluid, bone, soft tissue and air. These probabilistic images were then smoothed (5mm full width half maximum), thresholded and resliced to produce binary masks of 2mm × 2mm × 2mm resolution for three tissue types: brain (including grey matter, white matter and cerebrospinal fluid), skull and scalp. These binary masks were transformed to hexahedral meshes with FieldTrip[123]. All three considered tissue types were assumed to have homogeneous and isotropic conductivity: 330 ms/m for the brain and scalp[125], and an age-dependent skull conductivity of $3.958 + 62.77 \times e^{-0.2404 \times \text{age in years}}$ ms/m, in line with the BESA[126] recommended conductivity ratios. Segmentations were visually inspected. The forward model was derived with FieldTrip and SimBio[127]. For the inverse model, 1200 source locations of interest were defined in grey matter in Montreal Neurological Institute (MNI) space, following a 3D cubic diamond grid. Source positions were transformed from MNI space to each subject's individual space with a nonlinear transformation using SPM12. Electrode positions were determined by transforming standard MNI positions to subject-space with the same transformation, then projecting to the scalp surface. Source time series were estimated with linearly constrained minimum variance beamformer[36], using a regularization of 5% of the average trace of the covariance

matrix. The 1200 sources were parcelled into 68 cortical regions of interest, as per the Desikan-Killiany atlas[46]. Each region was comprised of between 1 and 67 sources (median = 13). When there was more than one source per region, the representative time series for a given region was defined as the first principal component of all the source time series in it.

Cropping, down-sampling and filtering

We chose 20 second eyes-closed resting-state EEG epochs (from a maximum segment length of 30 seconds) to produce functional connectivity adjacency matrices. This epoch length was chosen as a compromise between maximising the number of included participants and maximising network stability[128,129].

We then further down-sampled the signals to 250Hz. Data quality checks were subsequently performed.

We treated the whole 20 second epoch as a single window. Producing multiple windows has the advantage of better capturing moment-to-moment connectivity. However, longer window-length better captures the 'ground truth'[129]. Additionally, longer windows are needed to capture weaker connections[129] due to the noise inherent to EEG signals.

The signals were then filtered into the conventional frequency bands: delta (1-4 Hz), theta (4-8 Hz), alpha (8-13 Hz), low-beta (13-20 Hz) and high-beta (20-32 Hz). High-pass followed by low-pass filters were used in sequence, using two-pass (using the MATLAB function filtfilt), finite impulse response filters, of order 250. To reduce signal distortion, data padding of 500 samples (2 seconds) was used during filtering and while performing Hilbert transformations.

Quantifying phase-delays

To quantify the phase-delay between two signals $x_i\,(t)$ and $x_j(t)$, $t\ =\ 1, \ldots., N$ where N is the number of points in an EEG epoch, we first applied the Hilbert transform to obtain the instantaneous phases $\theta_i(t), \theta_j(t)$ for the signals $x_i\,(t)$ and $x_j(t)$ respectively. Then, the phase-delay distribution $\Delta\theta(t) =\ \theta_i(t) - \theta_j(t)$ was projected into the unit circle. The instantaneous phase-delays across samples in an epoch were averaged to produce the mean phase-delay throughout the epoch:

$$\tau_{i,j} =\ angle(\frac{1}{N}\sum_{t=1}^{N} e^{\mathrm{i}*\Delta\theta(\mathrm{t})})$$

Investigating where the effects of signal leakage are likely negligible

We graphically examined the relationship between the proportion of zero and near-zero phase-delay functional connectivity and Euclidean distance between region pairs. Artefactual connectivity due to signal leakage occurs at zero-phase-delay[31,51] and its influence is a function of Euclidean distance between sources[31,37,50,51]. Therefore, we explored if there was a Euclidean distance beyond which the proportion of zero- and near-zero phase-delay connectivity did not vary with increasing distance. Such a

phenomena would suggest that artefactual connectivity due to signal leakage is likely negligible beyond this Euclidean distance.

Euclidean distance between region-pairs was measured from the centroids of the regions, obtained from the FreeSurfer surface parcellation, measured per participant using individual T1w MRI images.

In the absence of an established definition of 'near-zero-phase-delay' functional connectivity, we defined near-zero-phase-delay as within < | 0.3 | radians from 0 or ±π radians. These phase-delays comprise approximately 19% of possible phase-delays in a unit circle (between -π and π). For comparison, the phase delay caused by signal transmission delays along a (white matter) streamline of length 128mm (the median length between region-pairs in our dataset), assuming a white matter transmission speed of 4.5m/s[97] and a synaptic transmission delay of 0.75 milliseconds[130], for oscillations at 10 Hz, is approximately 1.83 radians. Note that by design, all zero-phase-exclusive methods alter the functional connectivity value based on how close phase-delay is to 0 or π. Connectivity strength values are only unaltered by zero-phase-exclusive methods at phase delays of ±π/2 radians, and approach zero as phase-delay approaches 0 or ±π. At phase delays of 0.3 radians, the measured connectivity strength of 'true' (and artefactual) functional connectivity is decreased by 70% using the wPLI and Img COH compared to when using zero-phase-inclusive methods.

Functional Connectivity Methods

Coherence and imaginary part of coherency

Coherence measures the consistency of relative amplitude and phase between pairs of signals at a given frequency.

Coherence is the absolute value of coherency, $C_{ij}(f)$, between signals i and j, defined as:

$$C_{ij}(f) \equiv \frac{S_{ij}(f)}{(S_{ii}(f)S_{jj}(f))^{1/2}}$$

Where $S_{ij}(f)$ is the cross spectral density of signals i and j, $S_{ii}(f)$ is the power spectral density of signal i, and $S_{jj}(f)$ is the power spectral density of signal j. We used the Welch method to calculate power spectral density, as it has the advantage of handling signal leakage effects well[132].

Therefore, coherence $\mathrm{Coh}_{ij}(f)$, is:

$$Coh_{ij}(f) \equiv \left| \frac{S_{ij}(f)}{(S_{ii}(f)S_{jj}(f))^{1/2}} \right|$$

The imaginary part of coherency only considers the imaginary component of the complex-valued cross spectral density:

$$Img\ Coh_{ij}(f)\ \equiv |\frac{Img(S_{ij}(f))}{(S_{ii}(f)S_{jj}(f))^{1/2}}|$$

Phase Locking value

Phase-based connectivity methods assume that two brain regions are connected if the rhythm of their oscillations are similar, largely independent of amplitude relationships.

The phase locking value between the signals $x_i\ (t)$ and $x_j(t)$, $t\ =\ 1, \ldots., N$ where N is the number of points in an epoch is defined as:

$$PLV_{ij}\ =\ \frac{1}{N}\left|\sum_{t=1}^{N} e^{i*\Delta\theta(t)}\right|$$

Where $\Delta\theta(t)$ is the difference of the instantaneous phases $\theta_i\ (t), \theta_j(t)$ of the signals $x_i(t), x_j(j)$. Here, we did not perform the permutation testing that is typical for the PLV[55], to enable comparisons with the other structural and functional connectivity methods used in this analysis.

Weighted Phase Lag Index

The weighted phase lag index is derived by multiplying the phase lag index value by a multiplier based on the amplitude of the phase-difference.

The weighted phase lag index between two signals i and j is defined as:

$$wPLI_{ij}\ \equiv \frac{\left|E\left\{Im\left(S_{ij}(f)\right)\right\}\right|}{E\left\{\left|Im\left(S_{ij}(f)\right)\right|\right\}} = \frac{|E\{\left|Im\left(S_{ij}(f)\right)\right| sgn(Im(S_{ij}(f)))\}|}{E\left\{\left|Im\left(S_{ij}(f)\right)\right|\right\}}$$

where S_{ij} is the cross spectrum between the signals i and j.

Amplitude envelope correlation and orthogonalized amplitude envelope correlation

The amplitude envelope correlation (AEC) detects amplitude relationships between signals, independent of phase relationships. The AEC between region-pairs i and j is the magnitude of the Pearson correlation coefficient between the absolute values of Hilbert transformed signal i and the absolute values of Hilbert transformed signal j.

In the orthogonalized AEC, pairs of signals are orthogonalized with respect to each other prior to carrying out the AEC calculation. Orthogonalization was performed (on a per-sample basis) in two directions (i to j, j to i), producing $i_{\perp j}$ and $j_{\perp i}$ timeseries, as per[31]. $i_{\perp j}$, for example was derived by:

$$i_{\perp j}(t,f) = i(t,f) -\ i_{||j}(t,f),$$

when

$$i_{||j}(t,f) =\ a_{i,j}(f,T)j(t,f)$$

Where $a_{i,j}$ is the regression coefficient obtained by ordinary least squares describing the linear relationship between i and j throughout the epoch (t = 20). The orthogonalized time series were then squared and log transformed, to make the time series more normal, as per[31]. Then, power envelope correlations were computed between i and $j_{\perp i}$, and j and $i_{\perp j}$ – the mean of the two correlation values was taken to be the undirected orthogonalized connectivity value between i and j.

Test-retest reliability

We quantified the intrasession test-retest reliability between two epochs recorded between 1-3 minutes of each other. Intrasession test-retest reliability was used to reduce the confounding effects of circadian rhythm[133] and caffeine[134] on functional connectivity. Two measures of test-retest reliability were used: absolute agreement and consistency. Edgewise absolute agreement was quantified using the interclass correlation coefficient (ICC (2,1)). ICC values were interpreted as per[135]: 0.9 -1.0 indicate excellent reliability, 0.75-0.9 indicate good reliability, 0.5-0.75 indicate moderate reliability and 0.0-0.5 indicate poor reliability. Negative values were given a value of 0. We quantified the consistency of the whole adjacency matrix using Spearman's correlation coefficient, as per[62].

Structure–function concordance

Structural connectivity between 68 grey matter regions, as parcellated by the Desikan-Killiany atlas[46], was quantified by using spherical deconvolution diffusion weighted imaging. Spherical deconvolution diffusion imaging was used to overcome the crossing fibres problem that is a key limitation of traditional diffusion tensor imaging[94]. Connectivity strength between two regions was based on the streamline count between them, normalised to the value of 1, as per[63]. Structure-function concordance was calculated on a per-participant basis, using Spearman's correlation coefficient. Diffusion imaging data was available from 2 of 5 study sites (KCL and Mannheim), comprising 50 participants (Table 3a).

T1-weighted cortical reconstruction using FreeSurfer

Signals from diffusion imaging were projected on to the cortical surface derived from each participant's T1w MRI image as per[136]. All T1 scans were manually inspected; those with visible anomalies or significant movement artefacts were excluded. For each T1w MRI, models of the cortical surface using FreeSurfer v6.0 (https://surfer.nmr.mgh.harvard.edu/) were computed. A detailed description of these well-validated and automated procedures is provided here[137]. In brief, FreeSurfer performs intensity normalization, skull stripping, and an image segmentation using a connected-components algorithm. Next, it generates a filled white matter volume for each hemisphere and, by fitting a deformable template, a surface tessellation for each of these volumes. For each subject, this yields a mesh (of triangular elements) for the inner (white-matter) and outer (pial) cortical surface consisting of ~150k vertices (points in each triangular element) per hemisphere. Each of these reconstructed surfaces was inspected visually for reconstruction errors by three independent and experienced researchers. Scans were either accepted or manually edited after automatic pre-processing. Manually edited images were iteratively re-pre-processed and visually re-assessed.

Table 3a – demographics of participants who had both EEG and diffusion weighted imaging data. FSIQ: full scale intellectual quotient

Participants	KCL n = 28	Mannheim n = 22
Mean Age (SD)	23 (4.7)	15 (2.9)
Age Range	15 - 31	8 - 19
Mean FSIQ (SD)	109 (13.3)	110 (13.3)
FSIQ Range	85 – 142	77 – 133

Table 3b. Diffusion MRI acquisition parameters

	KCL	Mannheim
Scanner	GE MR750	Siemens TimTrio
Sequence	SE-EPI	SE-EPI
Field of view	256×256 mm^2	256×256 mm^2
Matrix size	128×128	128×128
Number of slices	72	72
Voxel size	$2 \times 2 \times 2$ mm^3	$2 \times 2 \times 2$ mm^3
Echo time	67 ms	102 ms
Repetition time	12 s	12 s
Flip angle	90	90
B-value	1500 s/mm^2	1500 s/mm^2
Diffusion directions	60	60
No. b=0 images	6	6

Diffusion MRI pre-processing

Diffusion MRI acquisition parameters are detailed in Table 3b. Tools from Connectome Workbench (https://www.humanconnectome.org/software) were used to re-tessellate the T1w surfaces of each participant to the common tessellation of the '32k_FS_LR' template. This was done to reduce the number of vertices in each surface to 32,492 points, reducing the computational burden of the cortical projection step.

The diffusion series of each participant was corrected for thermal noise[138] and Gibbs ringing artefacts[139]. Due to the lack of reversed phase encoding images, the *SynB0* framework[140] was used to generate undistorted b=0 EPIs and these were used to estimate the susceptibility distortion field using *topup*[141]. Next, *eddy* was used to correct the diffusion series for artefacts caused by frame-wise motion and eddy currents[142], intra-frame motion[143], and signal dropout[144], as well as susceptibility distortions using the field generated by *topup*. The anisotropic map[145] was generated from the corrected data and used to calculate a rigid-body registration of the diffusion data to the subject's T1w structural image in FLIRT[146], and this transformation was applied to the entire diffusion series with a spline interpolation to align it with the T1w image; the bvecs were rotated with the same affine matrix.

Tractography and structural connectivity

Diffusion modelling was performed using the damped Richardson-Lucy spherical deconvolution algorithm[147] in *StarTrack* (https://mr-startrack.com), with the following parameters: fibre response $\alpha = 1.5$; number of iterations = 300; amplitude threshold $\eta = 0.0015$; geometric regularisation $v = 16$. Fibre tracking was performed with the Euler-type algorithm according to the following parameters: minimum HMOA threshold = 0.002; maximum angle threshold = 45°; step size = 1 mm; minimum fibre length = 20 mm; maximum fibre length = 300 mm.

Each participant's resulting tractogram was then converted to a connectivity matrix, as done previously[148]. In brief, each streamline was projected to its nearest neighbouring vertex along the grey-white matter boundary surface (obtained from *FreeSurfer*) with a maximum distance of 3 mm. This resulted in a vertex-wise matrix, which was collapsed into a smaller matrix based on the Desikan-Killiany cortical parcellation[46]. Several parcel-wise connectivity matrices were produced with the following edge weights: streamline count; log-transformed streamline count; hindrance modulated orientational anisotropy (HMOA)[94], a tract-specific measure of white matter microstructure; and median fibre length.

Predicting age

We assessed the ability of mean strength derived from each functional connectivity method to predict current age over and above head circumference. First, we calculated the R^2 from 10-fold cross-validation using head circumference as the only predictor of current age (model 1). Then, we added mean strength this model (model 2). We used the change in R^2 (model 2 – model 1) as the quantity of interest. 147 participants had head circumference data. We excluded two outlier values (90cm from a 22-year-old and 66cm from a 13-year-old) as these likely reflected measurement inaccuracies.

We assessed if model 2 – model 1 cross-validation R^2 between methodologically corresponding zero-phase inclusive and exclusive methods (e.g. PLI versus wPLI) were significantly different using permutation testing. We created a null distribution by permuting age 1000 times for each method-pair in each frequency band.

Prognostic ability for longitudinal changes in spatial working memory

Spatial working memory was measured using the 'Find the Phone' Task[149,150]. In this task, multiple telephones were shown on a computer screen and 'rang' one at a time. Through trial and error, participants had to guess which phone was ringing. Participants were instructed that each phone would only ring once within a trial. The task was to remember which telephone(s) had already rung to avoid re-selecting that phone. Instances where a participant selected a phone that had already rung, or had previously been incorrectly selected, were counted as errors. The metric of interest was 'total participant errors.'

Weighted, normalised pathlength derived from functional connectivity, in the theta band, was used as the candidate prognostic biomarker. We only looked at connectivity between region-pairs with a strong evidence-base of being implicated in spatial working memory, including regions in the prefrontal cortex[82,85–87], the posterior parietal cortex[83,85], the anterior cingulate cortex[87], and the entorhinal cortex[83,84], as defined by the Desikan-Killiany atlas[46]. In total, there were 14 regions of interest in each hemisphere. Shorter weighted, normalised pathlengths reflect higher network efficiency. Global network efficiency and pathlength have been associated with working memory performance[79,80].

To calculate weighted, normalised pathlength, we first created weighted, undirected functional connectivity adjacency matrices (networks) with 28 nodes. One matrix was created per functional connectivity method. Each node corresponded to a cortical region of the Desikan-Killiany atlas implicated in spatial working memory, while the weighted edges were the functional connectivity strengths between pairs of nodes. Next, using the MATLAB brain connectivity toolbox[151], we inverted network edges to lengths (edges with larger weights produce shorter lengths). Then, we computed the *shortest possible* distance between all pairs of nodes. Finally, we calculated the average shortest distance between all pair of nodes to produce the weighted normalised pathlength. Formally, the shortest weighted path length d_{ij} between any two nodes, e.g. i and j is defined as:

$$d_{i,j}^{w} = \sum_{w_{ij} \in gi \leftrightarrow j} w_{ij},$$

where $gi \leftrightarrow j$ is the shortest weighted path between nodes i and j.

The weighted, average shortest pathlength (L) between node i and all other nodes of the network is defined as:

$$L_i = \frac{\sum_{i \neq j} d_{i,j}^{w}}{(N-1)} ,$$

where N is the number of nodes (28 in this analysis) and $d_{i,j}$ is the shortest path length between nodes i and j, when j is any node that is not i.

To calculate the normalised weighted pathlength, we used a normalisation process by creating 500 random networks by randomising the empirical network, while preserving the degree and strength distributions: each edge was rewired 5 times, with edge weights randomised every 5th step. The weighted pathlength of each random network was calculated, and then averaged across each of the 500 random networks to produce L_{rand}. The normalised average shortest pathlength of node i was calculated as:

$$L_i{}' = \frac{L_i}{L_{rand}}$$

$L_i{}'$ at each node was averaged across 28 nodes to produce the mean normalised, weighted pathlength (referred to as normalised, weighted pathlength).

Penalisation Scale

We created a penalisation scale to quantify how connectivity values would be altered by zero-phase-exclusive methods. The scale was between 0 and 1, where the most penalizable phase differences (0 and ±π) were given a value of 1 and least penalizable phase differences (±π/2) were given a value of 0. Penalisation scale values were calculated as follows:

$$Penalisation\ value = \frac{\left|\left|\text{average phase delay}\right| - \frac{\pi}{2}\right|}{\frac{\pi}{2}}$$

Where the average absolute phase delay was limited between 0 and +π. To examine if stronger structural connections were more likely to be associated with more penalizable phase-delays, we spearman correlated the penalisation values with the structural connectivity matrix on a per-participant basis. This was only done for region-pairs between which there were 1 or more streamlines.

Bootstrapping for mediation effects

We performed a mediation analysis to investigate if the association between structural connectivity strength and the penalisability of the phase-difference of functional connectivity was mediated by a proxy for white matter signal transmission time. We tested the significance of the indirect effect using bootstrapping procedures. Unstandardized indirect effects were computed for each of 1000 bootstrapped

samples, and the 95% confidence interval was computed by determining the indirect effects at the 2.5th and 97.5th percentiles.

Acknowledgments

We are grateful to Dr Piotr J. Franaszczuk for his expert advice on signal analysis and filtering and to Prof Dr Christine Ecker and team for pre-processing the T1-weighted MRI images.

Data availability

The LEAP Study data is available here, subject to an approved data application: https://redcap.pasteur.fr/surveys/?s=YRFF78PH89

References

1. Buzsáki, G. Theta oscillations in the hippocampus. *Neuron* **33**, 325–340 (2002).
2. Bishop, Geo. H. Cyclic changes in the excitability of the optic pathway of the rabbit. *American Journal of Physiology* **103**, 213–224 (1932).
3. Lopes da Silva, F. EEG and MEG: Relevance to neuroscience. *Neuron* **80**, 1112–1128 (2013).
4. Buzsáki, G. *Rhythms of the Brain*. (Oxford Academic, New York, 2006).
5. Womelsdorf, T. & Fries, P. The role of neuronal synchronization in selective attention. *Curr Opin Neurobiol* **17**, 154–160 (2007).
6. Rodriguez, E. *et al.* Perception's shadow: long-distance synchronization of human brain activity. *Nature 1999 397:6718* **397**, 430–433 (1999).
7. Uhlhaas, P. J. *et al.* Neural synchrony in cortical networks: history, concept and current status. *Front Integr Neurosci* **3**, (2009).
8. Singer, W. Neuronal Synchrony: A Versatile Code for the Definition of Relations? *Neuron* **24**, 49–65 (1999).
9. Varela, F., Lachaux, J. P., Rodriguez, E. & Martinerie, J. The brainweb: phase synchronization and large-scale integration. *Nat Rev Neurosci* **2**, 229–239 (2001).
10. Kang, S. S., Sponheim, S. R., Chafee, M. V. & MacDonald, A. W. Disrupted functional connectivity for controlled visual processing as a basis for impaired spatial working memory in schizophrenia. *Neuropsychologia* **49**, 2836–2847 (2011).
11. Dai, Z. *et al.* EEG Cortical Connectivity Analysis of Working Memory Reveals Topological Reorganization in Theta and Alpha Bands. *Front Hum Neurosci* **11**, (2017).
12. Hampson, M., Driesen, N. R., Skudlarski, P., Gore, J. C. & Constable, R. T. Brain Connectivity Related to Working Memory Performance. *The Journal of Neuroscience* **26**, 13338 (2006).
13. Du, Y., Fu, Z. & Calhoun, V. D. Classification and prediction of brain disorders using functional connectivity: Promising but challenging. *Front Neurosci* **12**, 373866 (2018).
14. Plitta, M., Barnes, K. A., Wallace, G. L., Kenworthy, L. & Martin, A. Resting-state functional connectivity predicts longitudinal change in autistic traits and adaptive functioning in autism. *Proc Natl Acad Sci U S A* **112**, E6699–E6706 (2015).
15. Gholipour, T. *et al.* Common functional connectivity alterations in focal epilepsies identified by machine learning. *Epilepsia* **63**, 629 (2022).
16. Gil Ávila, C. *et al.* DISCOVER-EEG: an open, fully automated EEG pipeline for biomarker discovery in clinical neuroscience. *Scientific Data 2023 10:1* **10**, 1–14 (2023).

17. Gao, Y. *et al.* Functional connectivity of white matter as a biomarker of cognitive decline in Alzheimer's disease. *PLoS One* **15**, e0240513 (2020).
18. Hong, S. J. *et al.* Toward a connectivity gradient-based framework for reproducible biomarker discovery. *Neuroimage* **223**, 117322 (2020).
19. Engel, A. K., Gerloff, C., Hilgetag, C. C. & Nolte, G. Intrinsic coupling modes: multiscale interactions in ongoing brain activity. *Neuron* **80**, 867–886 (2013).
20. Friston, K. J. Functional and Effective Connectivity: A Review. *Brain Connect* **1**, (2011).
21. O'Reilly, C. & Elsabbagh, M. Intracranial recordings reveal ubiquitous in-phase and in-antiphase functional connectivity between homotopic brain regions in humans. *J Neurosci Res* **99**, 887–897 (2021).
22. Witham, C. L., Wang, M. & Baker, S. N. Cells in somatosensory areas show synchrony with beta oscillations in monkey motor cortex. *Eur J Neurosci* **26**, 2677–2686 (2007).
23. Vicente, R., Gollo, L. L., Mirasso, C. R., Fischer, I. & Pipa, G. Dynamical relaying can yield zero time lag neuronal synchrony despite long conduction delays. *Proc Natl Acad Sci U S A* **105**, 17157–17162 (2008).
24. Engel, A. K., König, P., Kreiter, A. K. & Singer, W. Interhemispheric Synchronization of Oscillatory Neuronal Responses in Cat Visual Cortex. *Science (1979)* **252**, 1177–1179 (1991).
25. Gollo, L. L., Mirasso, C., Sporns, O. & Breakspear, M. Mechanisms of Zero-Lag Synchronization in Cortical Motifs. *PLoS Comput Biol* **10**, e1003548 (2014).
26. Rodriguez, E. *et al.* Perception's shadow: long-distance synchronization of human brain activity. *Nature 1999 397:6718* **397**, 430–433 (1999).
27. Gray, C. M., König, P., Engel, A. K. & Singer, W. Oscillatory responses in cat visual cortex exhibit inter-columnar synchronization which reflects global stimulus properties. *Nature 1989 338:6213* **338**, 334–337 (1989).
28. Roelfsema, P. R., Engel, A. K., König, P. & Singer, W. Visuomotor integration is associated with zero time-lag synchronization among cortical areas. *Nature 1997 385:6612* **385**, 157–161 (1997).
29. Steinmetz, P. N. *et al.* Attention modulates synchronized neuronal firing in primate somatosensory cortex. *Nature 2000 404:6774* **404**, 187–190 (2000).
30. O'Keefe, J. & Recce, M. L. Phase relationship between hippocampal place units and the EEG theta rhythm. *Hippocampus* **3**, 317–330 (1993).
31. Hipp, J. F., Hawellek, D. J., Corbetta, M., Siegel, M. & Engel, A. K. Large-scale cortical correlation structure of spontaneous oscillatory activity. *Nature Neuroscience 2012 15:6* **15**, 884–890 (2012).
32. Brunner, C. *et al.* Volume conduction influences scalp-based connectivity estimates. *Front Comput Neurosci* **10**, 212359 (2016).
33. Nolte, G. *et al.* Identifying true brain interaction from EEG data using the imaginary part of coherency. *Clinical Neurophysiology* **115**, 2292–2307 (2004).
34. Srinivasan, R., Winter, W. R., Ding, J. & Nunez, P. L. EEG and MEG coherence: measures of functional connectivity at distinct spatial scales of neocortical dynamics. *J Neurosci Methods* **166**, 41 (2007).
35. Colclough, G. L., Brookes, M. J., Smith, S. M. & Woolrich, M. W. A symmetric multivariate leakage correction for MEG connectomes. *Neuroimage* **117**, 439 (2015).
36. Anzolin, A. *et al.* Quantifying the Effect of Demixing Approaches on Directed Connectivity Estimated Between Reconstructed EEG Sources. *Brain Topogr* **32**, 655–674 (2019).

37. Bastos, A. M. & Schoffelen, J. M. A tutorial review of functional connectivity analysis methods and their interpretational pitfalls. *Front Syst Neurosci* **9**, 165147 (2016).
38. Colclough, G. L. *et al.* How reliable are MEG resting-state connectivity metrics? *Neuroimage* **138**, 284 (2016).
39. Miljevic, A., Bailey, N. W., Vila-Rodriguez, F., Herring, S. E. & Fitzgerald, P. B. Electroencephalographic Connectivity: A Fundamental Guide and Checklist for Optimal Study Design and Evaluation. *Biol Psychiatry Cogn Neurosci Neuroimaging* **7**, 546–554 (2022).
40. Cociu, B. A. *et al.* Multimodal functional and structural brain connectivity analysis in autism: A preliminary integrated approach with EEG, fMRI, and DTI. *IEEE Trans Cogn Dev Syst* **10**, 213–226 (2018).
41. O'Reilly, C., Lewis, J. D. & Elsabbagh, M. Is functional brain connectivity atypical in autism? A systematic review of EEG and MEG studies. *PLoS One* **12**, (2017).
42. Davis, K. D. *et al.* Discovery and validation of biomarkers to aid the development of safe and effective pain therapeutics: challenges and opportunities. *Nature Reviews Neurology 2020 16:7* **16**, 381–400 (2020).
43. Silver Spring (MD): Food and Drug Administration (US); Bethesda (MD): National Institutes of Health (US). BEST (Biomarkers, EndpointS, and other Tools) Resource. *BEST (Biomarkers , EndpointS , and other Tools) Resource* (2016).
44. Loth, E. *et al.* The EU-AIMS Longitudinal European Autism Project (LEAP): design and methodologies to identify and validate stratification biomarkers for autism spectrum disorders. *Mol Autism* **8**, (2017).
45. Charman, T. *et al.* The EU-AIMS Longitudinal European Autism Project (LEAP): Clinical characterisation. *Mol Autism* **8**, 27 (2017).
46. Desikan, R. S. *et al.* An automated labeling system for subdividing the human cerebral cortex on MRI scans into gyral based regions of interest. *Neuroimage* **31**, 968–980 (2006).
47. Ni, Z. *et al.* Two phases of interhemispheric inhibition between motor related cortical areas and the primary motor cortex in human. *Cereb Cortex* **19**, 1654–1665 (2009).
48. Palmer, L. M. *et al.* The cellular basis of GABA(B)-mediated interhemispheric inhibition. *Science* **335**, 989–993 (2012).
49. Hilgetag, C. C., Théoret, H. & Pascual-Leone, A. Enhanced visual spatial attention ipsilateral to rTMS-induced 'virtual lesions' of human parietal cortex. *Nature Neuroscience 2001 4:9* **4**, 953–957 (2001).
50. He, B. *et al.* Electrophysiological Brain Connectivity: Theory and Implementation. *IEEE Trans Biomed Eng* **66**, 2115–2137 (2019).
51. Gohel, B., Lee, P., Kim, M. Y., Kim, K. & Jeong, Y. MEG Based Functional Connectivity: Application of ICA to Alleviate Signal Leakage. *IRBM* **38**, 127–137 (2017).
52. Conturo, T. E. *et al.* Tracking neuronal fiber pathways in the living human brain. *Proc Natl Acad Sci U S A* **96**, 10422–10427 (1999).
53. Cauda, F. *et al.* Interhemispheric co-alteration of brain homotopic regions. *Brain Struct Funct* **226**, 2181 (2021).
54. Stam, C. J. & van Straaten, E. C. W. Go with the flow: Use of a directed phase lag index (dPLI) to characterize patterns of phase relations in a large-scale model of brain dynamics. *Neuroimage* **62**, 1415–1428 (2012).
55. Lachaux, J. P., Rodriguez, E., Martinerie, J. & Varela, F. J. Measuring phase synchrony in brain signals. *Hum Brain Mapp* **8**, 194 (1999).

56. Bruns, A., Eckhorn, R., Jokeit, H. & Ebner, A. Amplitude envelope correlation detects coupling among incoherent brain signals. *Neuroreport* **15**, 1509–1514 (2000).
57. Adey, W. R., Elul, R., Walter, R. D. & Crandall, P. H. The cooperative behavior of neuronal populations during sleep and mental tasks. *Electroencephalogr Clin Neurophysiol* (1967).
58. Vinck, M., Oostenveld, R., Van Wingerden, M., Battaglia, F. & Pennartz, C. M. A. An improved index of phase-synchronization for electrophysiological data in the presence of volume-conduction, noise and sample-size bias. *Neuroimage* **55**, 1548–1565 (2011).
59. Bullmore, E. & Sporns, O. The economy of brain network organization. *Nature Reviews Neuroscience 2012 13:5* **13**, 336–349 (2012).
60. Finger, H. *et al.* Modeling of Large-Scale Functional Brain Networks Based on Structural Connectivity from DTI: Comparison with EEG Derived Phase Coupling Networks and Evaluation of Alternative Methods along the Modeling Path. *PLoS Comput Biol* **12**, e1005025 (2016).
61. Fraschini, M., Pani, S. M., Didaci, L. & Marcialis, G. L. Robustness of functional connectivity metrics for EEG-based personal identification over task-induced intra-class and inter-class variations. *Pattern Recognit Lett* **125**, 49–54 (2019).
62. van der Velde, B., Haartsen, R. & Kemner, C. Test-retest reliability of EEG network characteristics in infants. *Brain Behav* **9**, (2019).
63. Chu, C. J. *et al.* EEG functional connectivity is partially predicted by underlying white matter connectivity. *Neuroimage* **108**, 23–33 (2015).
64. Baum, G. L. *et al.* Development of structure–function coupling in human brain networks during youth. *Proc Natl Acad Sci U S A* **117**, 771–778 (2020).
65. Honey, C. J. *et al.* Predicting human resting-state functional connectivity from structural connectivity. *Proc Natl Acad Sci U S A* **106**, 2035–2040 (2009).
66. Fotiadis, P. *et al.* Structure–function coupling in macroscale human brain networks. *Nature Reviews Neuroscience 2024* 1–17 (2024) doi:10.1038/s41583-024-00846-6.
67. Jovicich, J. *et al.* Reliability in multi-site structural MRI studies: Effects of gradient non-linearity correction on phantom and human data. *Neuroimage* **30**, 436–443 (2006).
68. Mancuso, L. *et al.* The homotopic connectivity of the functional brain: a meta-analytic approach. *Scientific Reports 2019 9:1* **9**, 1–19 (2019).
69. Schmahmann, J. D. & Pandya, D. N. Fiber Pathways of the Brain. *Fiber Pathways of the Brain* 1–654 (2009) doi:10.1093/ACPROF:OSO/9780195104233.001.0001.
70. Fair, D. A. *et al.* Functional Brain Networks Develop from a “Local to Distributed” Organization. *PLoS Comput Biol* **5**, e1000381 (2009).
71. Collin, G. & Van Den Heuvel, M. P. The ontogeny of the human connectome: development and dynamic changes of brain connectivity across the life span. *Neuroscientist* **19**, 616–628 (2013).
72. Edde, M., Leroux, G., Altena, E. & Chanraud, S. Functional brain connectivity changes across the human life span: From fetal development to old age. *J Neurosci Res* **99**, 236–262 (2021).
73. Pletcher, M. J. & Pignone, M. Evaluating the Clinical Utility of a Biomarker: A Review of Methods for Estimating Health Impact. *Circulation* **123**, 1116 (2011).
74. Fox, M. D. *et al.* The human brain is intrinsically organized into dynamic, anticorrelated functional networks. *Proc Natl Acad Sci U S A* **102**, 9673–9678 (2005).

75. Dai, Z. *et al.* Eeg cortical connectivity analysis of working memory reveals topological reorganization in theta and alpha bands. *Front Hum Neurosci* **11**, 237 (2017).
76. Alloway, T. P., Rajendran, G. & Archibald, L. M. D. Working Memory in Children With Developmental Disorders. *J Learn Disabil* **42**, 372–382 (2009).
77. Gathercole, S. E. & Alloway, T. P. Practitioner review: short-term and working memory impairments in neurodevelopmental disorders: diagnosis and remedial support. *J Child Psychol Psychiatry* **47**, 4–15 (2006).
78. Chai, W. J., Abd Hamid, A. I. & Abdullah, J. M. Working memory from the psychological and neurosciences perspectives: A review. *Front Psychol* **9**, 327922 (2018).
79. Langer, N., von Bastian, C. C., Wirz, H., Oberauer, K. & Jäncke, L. The effects of working memory training on functional brain network efficiency. *Cortex* **49**, 2424–2438 (2013).
80. Stanley, M. L. *et al.* Changes in Brain Network Efficiency and Working Memory Performance in Aging. *PLoS One* **10**, (2015).
81. Jones, M. W. & Wilson, M. A. Theta Rhythms Coordinate Hippocampal–Prefrontal Interactions in a Spatial Memory Task. *PLoS Biol* **3**, e402 (2005).
82. Siapas, A. G., Lubenov, E. V. & Wilson, M. A. Prefrontal phase locking to hippocampal theta oscillations. *Neuron* **46**, 141–151 (2005).
83. Almeida, R., Barbosa, J. & Compte, A. Neural circuit basis of visuo-spatial working memory precision: a computational and behavioral study. *J Neurophysiol* **114**, 1806–1818 (2015).
84. Salimi, M. *et al.* The olfactory bulb modulates entorhinal cortex oscillations during spatial working memory. *Journal of Physiological Sciences* **71**, 1–9 (2021).
85. MacKey, W. E. & Curtis, C. E. Distinct contributions by frontal and parietal cortices support working memory. *Scientific Reports 2017 7:1* **7**, 1–7 (2017).
86. Wager, T. D. & Smith, E. E. Neuroimaging studies of working memory: A meta-analysis. *Cogn Affect Behav Neurosci* **3**, 255–274 (2003).
87. Wirt, R. A. & Hyman, J. M. Integrating Spatial Working Memory and Remote Memory: Interactions between the Medial Prefrontal Cortex and Hippocampus. *Brain Sciences 2017, Vol. 7, Page 43* **7**, 43 (2017).
88. Hyman, J. M., Zilli, E. A., Paley, A. M. & Hasselmo, M. E. Working memory performance correlates with prefrontal-hippocampal theta interactions but not with prefrontal neuron firing rates. *Front Integr Neurosci* **4**, 1162 (2010).
89. Fell, J. & Axmacher, N. The role of phase synchronization in memory processes. *Nature Reviews Neuroscience 2011 12:2* **12**, 105–118 (2011).
90. Bauer, M., Buckley, M. G. & Bast, T. Individual differences in theta-band oscillations in a spatial memory network revealed by electroencephalography predict rapid place learning. *Brain Neurosci Adv* **5**, 239821282110027 (2021).
91. Westerhausen, R. *et al.* Interhemispheric transfer time and structural properties of the corpus callosum. *Neurosci Lett* **409**, 140–145 (2006).
92. Whitford, T. J. *et al.* Predicting inter-hemispheric transfer time from the diffusion properties of the corpus callosum in healthy individuals and schizophrenia patients: A combined ERP and DTI study. *Neuroimage* **54**, 2318–2329 (2011).
93. Brookes, M. J., Woolrich, M. W. & Barnes, G. R. Measuring functional connectivity in MEG: A multivariate approach insensitive to linear source leakage. *Neuroimage* **63**, 910–920 (2012).
94. Dell'Acqua, F., Simmons, A., Williams, S. C. R. & Catani, M. Can spherical deconvolution provide more information than fiber orientations? Hindrance

modulated orientational anisotropy, a true-tract specific index to characterize white matter diffusion. *Hum Brain Mapp* **34**, 2464–2483 (2013).
95. Wang, X. *et al.* Assessment of peripheral neuropathy in type 2 diabetes by diffusion tensor imaging. *Quant Imaging Med Surg* **12**, 395–405 (2022).
96. Heckel, A. *et al.* Peripheral Nerve Diffusion Tensor Imaging: Assessment of Axon and Myelin Sheath Integrity. *PLoS One* **10**, e0130833 (2015).
97. van Blooijs, D. *et al.* Developmental trajectory of transmission speed in the human brain. *Nature Neuroscience 2023 26:4* **26**, 537–541 (2023).
98. Evstigneev, V. V, Kistsen, V. V & Bulaev, I. V. The Effect of Structural White Matter Abnormalities on the Clinical Course of Epilepsy.
99. Bassett, D. S. & Bullmore, E. T. Small-World Brain Networks Revisited. *Neuroscientist* **23**, 499–516 (2017).
100. Cabral, J. *et al.* Exploring mechanisms of spontaneous functional connectivity in MEG: How delayed network interactions lead to structured amplitude envelopes of band-pass filtered oscillations. *Neuroimage* **90**, 423–435 (2014).
101. Bauer, M., Buckley, M. G. & Bast, T. Individual differences in theta-band oscillations in a spatial memory network revealed by electroencephalography predict rapid place learning. *https://doi.org/10.1177/23982128211002725* **5**, 239821282110027 (2021).
102. Jian, W., Chen, M. & McFarland, D. J. EEG Based Zero-phase Phase-locking Value (PLV) and Effects of Spatial Filtering During Actual Movement. *Brain Res Bull* **130**, 156 (2017).
103. Mehrkanoon, S., Breakspear, M., Britz, J. & Boonstra, T. W. Intrinsic Coupling Modes in Source-Reconstructed Electroencephalography. *https://home.liebertpub.com/brain* **4**, 812–825 (2014).
104. Moran, R., Pinotsis, D. A. & Friston, K. Neural masses and fields in dynamic causal modelling. *Front Comput Neurosci* **7**, 44756 (2013).
105. Mill, R. D., Bagic, A., Bostan, A., Schneider, W. & Cole, M. W. Empirical validation of directed functional connectivity. *Neuroimage* **146**, 275–287 (2017).
106. Noble, S., Scheinost, D. & Constable, R. T. A guide to the measurement and interpretation of fMRI test-retest reliability. *Curr Opin Behav Sci* **40**, 27–32 (2021).
107. Calamante, F. The Seven Deadly Sins of Measuring Brain Structural Connectivity Using Diffusion MRI Streamlines Fibre-Tracking. *Diagnostics* **9**, (2019).
108. Jbabdi, S. & Johansen-Berg, H. Tractography: Where Do We Go from Here? *https://home.liebertpub.com/brain* **1**, 169–183 (2011).
109. Dennis, E. L. *et al.* Test-Retest Reliability of Graph Theory Measures of Structural Brain Connectivity. *Med Image Comput Comput Assist Interv* **15**, 305 (2012).
110. G.Carmines, E. & A.Zeller, R. Reliability and Validity Assessment. *Reliability and Validity Assessment* (1979) doi:10.4135/9781412985642.
111. Wolters, C. H., Anwander, A., Maess, B., MacLeod, R. S. & Friederici, A. D. The influence of volume conduction effects on the EEG/MEG reconstruction of the sources of the Early Left Anterior Negativity. *Conf Proc IEEE Eng Med Biol Soc* **2004**, 3569–3572 (2004).
112. Mclane, H. C. *et al.* Availability, accessibility, and affordability of neurodiagnostic tests in 37 countries. *Neurology* **85**, 1614 (2015).
113. Garcés, P. *et al.* Resting state EEG power spectrum and functional connectivity in autism: a cross-sectional analysis. *Molecular Autism 2022 13:1* **13**, 1–16 (2022).

114. Sato, J., Safar, K., Vogan, V. M. & Taylor, M. J. Functional connectivity changes during working memory in autism spectrum disorder: A two-year longitudinal MEG study. *Neuroimage Clin* **37**, 103364 (2023).
115. Musgrave, J. & Gloor, P. The role of the corpus callosum in bilateral interhemispheric synchrony of spike and wave discharge in feline generalized penicillin epilepsy. *Epilepsia* **21**, 369–378 (1980).
116. Bloom, J. S. & Hynd, G. W. The role of the corpus callosum in interhemispheric transfer of information: Excitation or inhibition? *Neuropsychol Rev* **15**, 59–71 (2005).
117. Contreras, D., Destexhe, A., Sejnowski, T. J. & Steriade, M. Control of spatiotemporal coherence of a thalamic oscillation by corticothalamic feedback. *Science* **274**, 771–774 (1996).
118. Gray, C. M. & McCormick, D. A. Chattering cells: superficial pyramidal neurons contributing to the generation of synchronous oscillations in the visual cortex. *Science* **274**, 109–113 (1996).
119. Kopell, N., Ermentrout, G. B., Whittington, M. A. & Traub, R. D. Gamma rhythms and beta rhythms have different synchronization properties. *Proc Natl Acad Sci U S A* **97**, 1867–1872 (2000).
120. Wechsler, D. Wechsler Abbreviated Scale of Intelligence--Second Edition. *APA PsycTests* https://psycnet.apa.org/doiLanding?doi=10.1037%2Ft15171-000 (2011).
121. Hyvärinen, A. Fast and robust fixed-point algorithms for independent component analysis. *IEEE Trans Neural Netw* **10**, 626–634 (1999).
122. Delorme, A. & Makeig, S. EEGLAB: An open source toolbox for analysis of single-trial EEG dynamics including independent component analysis. *J Neurosci Methods* **134**, 9–21 (2004).
123. Oostenveld, R., Fries, P., Maris, E. & Schoffelen, J. M. FieldTrip: Open Source Software for Advanced Analysis of MEG, EEG, and Invasive Electrophysiological Data. *Comput Intell Neurosci* **2011**, 156869 (2011).
124. Penny W, Friston K, John T. Ashburner J, Kiebel S & Nichols T. *Statistical Parametric Mapping: The Analysis of Functional Brain Images*. (2006).
125. Gabriel, S., Lau, R. W. & Gabriel, C. The dielectric properties of biological tissues: II. Measurements in the frequency range 10 Hz to 20 GHz. *Phys Med Biol* **41**, 2251–2269 (1996).
126. BESA® | Brain Electrical Source Analysis: Home. https://www.besa.de/.
127. Vorwerk, J., Oostenveld, R., Piastra, M. C., Magyari, L. & Wolters, C. H. The FieldTrip-SimBio pipeline for EEG forward solutions. *Biomed Eng Online* **17**, 1–17 (2018).
128. Fraschini, M. *et al.* The effect of epoch length on estimated EEG functional connectivity and brain network organisation. *J Neural Eng* **13**, (2016).
129. Pullon, R. M., Yan, L., Sleigh, J. W. & Warnaby, C. E. Granger Causality of the Electroencephalogram Reveals Abrupt Global Loss of Cortical Information Flow during Propofol-induced Loss of Responsiveness. *Anesthesiology* **133**, 774 (2020).
130. KATZ, B. & MILEDI, R. The measurement of synaptic delay, and the time course of acetylcholine release at the neuromuscular junction. *Proc R Soc Lond B Biol Sci* **161**, 483–495 (1965).
131. Pariz, A., Fischer, I., Valizadeh, A. & Mirasso, C. Transmission delays and frequency detuning can regulate information flow between brain regions. *PLoS Comput Biol* **17**, e1008129 (2021).

132. Welch, P. D. The Use of Fast Fourier Transform for the Estimation of Power Spectra: A Method Based on Time Averaging Over Short, Modified Periodograms. *IEEE Transactions on Audio and Electroacoustics* **15**, 70–73 (1967).
133. Fafrowicz, M. *et al.* Beyond the Low Frequency Fluctuations: Morning and Evening Differences in Human Brain. *Front Hum Neurosci* **13**, 477076 (2019).
134. Haller, S. *et al.* Acute caffeine administration impact on working memory-related brain activation and functional connectivity in the elderly: a BOLD and perfusion MRI study. *Neuroscience* **250**, 364–371 (2013).
135. Koo, T. K. & Li, M. Y. A Guideline of Selecting and Reporting Intraclass Correlation Coefficients for Reliability Research. *J Chiropr Med* **15**, 155–163 (2016).
136. Pretzsch, C. M. *et al.* Neurobiological Correlates of Change in Adaptive Behavior in Autism. *Am J Psychiatry* **179**, 336–349 (2022).
137. Fischl, B. FreeSurfer. *Neuroimage* **62**, 774–781 (2012).
138. Veraart, J., Fieremans, E. & Novikov, D. S. Diffusion MRI noise mapping using random matrix theory. *Magn Reson Med* **76**, 1582–1593 (2016).
139. Kellner, E., Dhital, B., Kiselev, V. G. & Reisert, M. Gibbs-ringing artifact removal based on local subvoxel-shifts. *Magn Reson Med* **76**, 1574–1581 (2016).
140. Schilling, K. G. *et al.* Synthesized b0 for diffusion distortion correction (Synb0-DisCo). *Magn Reson Imaging* **64**, 62–70 (2019).
141. Andersson, J. L. R., Skare, S. & Ashburner, J. How to correct susceptibility distortions in spin-echo echo-planar images: Application to diffusion tensor imaging. *Neuroimage* **20**, 870–888 (2003).
142. Andersson, J. L. R. & Sotiropoulos, S. N. An integrated approach to correction for off-resonance effects and subject movement in diffusion MR imaging. *Neuroimage* **125**, 1063–1078 (2016).
143. Andersson, J. L. R. *et al.* Towards a comprehensive framework for movement and distortion correction of diffusion MR images: Within volume movement. *Neuroimage* **152**, 450–466 (2017).
144. Andersson, J. L. R., Graham, M. S., Zsoldos, E. & Sotiropoulos, S. N. Incorporating outlier detection and replacement into a non-parametric framework for movement and distortion correction of diffusion MR images. *Neuroimage* **141**, 556–572 (2016).
145. (ISMRM 2014) Anisotropic Power Maps: A diffusion contrast to reveal low anisotropy tissues from HARDI data. https://archive.ismrm.org/2014/0730.html.
146. Jenkinson, M., Bannister, P., Brady, M. & Smith, S. Improved Optimization for the Robust and Accurate Linear Registration and Motion Correction of Brain Images. *Neuroimage* **17**, 825–841 (2002).
147. Dell'Acqua, F. *et al.* A modified damped Richardson–Lucy algorithm to reduce isotropic background effects in spherical deconvolution. *Neuroimage* **49**, 1446–1458 (2010).
148. Beyh, A. *et al.* The medial occipital longitudinal tract supports early stage encoding of visuospatial information. *Communications Biology 2022 5:1* **5**, 1–10 (2022).
149. Owen, A. M., Downes, J. J., Sahakian, B. J., Polkey, C. E. & Robbins, T. W. Planning and spatial working memory following frontal lobe lesions in man. *Neuropsychologia* **28**, 1021–1034 (1990).
150. Sjöwall, D., Roth, L., Lindqvist, S. & Thorell, L. B. Multiple deficits in ADHD: executive dysfunction, delay aversion, reaction time variability, and emotional deficits. *Journal of Child Psychology and Psychiatry* **54**, 619–627 (2013).

151. Rubinov, M., Kötter, R., Hagmann, P. & Sporns, O. Brain connectivity toolbox: a collection of complex network measurements and brain connectivity datasets. *Neuroimage* **47**, S169 (2009).